Phenomenological Regression Rate Model in Axial Injection End-Burning Hybrid Rocket Motor Using Different Oxidizers

Giuseppe Gallo[1], Mai Fukada[2], Sho Suzuki[3], Harunori Nagata[4]
Hokkaido University, Sapporo, Hokkaido, 060-8628, Japan

Abstract

Compared with conventional configurations, axial injection end-burning hybrid rocket motors work with multiport fuel grains, which mainly burn in the axial direction. The consumption rate is controlled by the several flames developed at the end of each port. Although many studies of performance and flame stability have been carried out in the past, a phenomenological model of the axial regression rate was never provided in the past, which is the objective of the current work. The validation of the physical model is performed by a comparative study between firing tests using gaseous oxygen and nitrous oxide. Two experimental campaigns performed by a pressure-controlled combustion chamber are carried out with a single port grain in operative conditions equivalent to the multiport configuration. The axial regression rate was measured by varying the port diameter in a range between 0.5 and 3 mm, the mass flow rate between 0.004 and 1.7 g/s, and the chamber pressure between 0.1 and 2.0 MPa. The measured axial regression rate was quantitatively lower with nitrous oxide than oxygen, and the pressure sensitivity exponent decreased from 1.85 to 1.5, respectively. The physical reason has been attributed to the decomposition reaction of nitrous oxide occurring upstream of the flame front. In addition, a general methodology for fuel grain design is given, highlighting the benefits and drawbacks of introducing multiport grains and the effect of the oxidizer choice on the motor geometry. Finally, multiport firing tests were carried out to confirm the evidence observed in the simplified single-port campaigns.

---

[1] JSPS International Fellow, Department of Space and Mechanical Engineering, Hokkaido University.

[2] PhD Student, Department of Mechanical and Space Engineering, Hokkaido University.

[3] PhD Student, Department of Mechanical and Space Engineering, Hokkaido University.

[4] Professor, Department of Mechanical and Space Engineering, and AIAA Member.

Nomenclature

A = area, m^2
A_s = PMMA pre-exponential constant, mm/s
c_p = specific heat at constant pressure, J/kg·K
D_{ext} = external nozzle diameter, m
D_p = port diameter, m
E_a = PMMA activation energy, J/K·mol
G = mass flux, kg/m^2·s
h = inter-port distance, m
H_v = total pyrolysis enthalpy, J/ kg
I = total impulse, N·s
Isp = specific impulse, m/s
k = thermal conductivity, W/ m·K
L_g = grain length, m
L_{ub} = unburnt grain length, m
$\dot{m}$ = mass flow rate, kg/s
M_w = molecular weight
N_p = number of ports
OF = mixture ratio
p = pressure, Pa
$\dot{q}$ = heat flux per unit of area, W/ m^2
$\dot{r}$ = regression rate, mm/s
R = universal gas constant
Re = Reynolds number
s = flame speed, m/s
Sc = Schmidt number
t_b = burning time, s
T = temperature, K
T_h = thrust, N
u = velocity, m/s
w = channel/fins width, m
x^* = stand-off distance, m
x_p = combustion flame stand-off distance, m
x_d = dissociation zone stand-off distance, m

Greek Symbols

μ = viscosity, kg/m·s
ρ = density, kg/m^3

Superscripts

$*$ = full configuration

Subscripts

$\perp$ = perpendicular
$\parallel$ = parallel
a = ambient
d = decomposition
f = fuel
g = gaseous
l = laminar
m = mixture
ox = oxidizer
r = radiative
s = surface
st = stoichiometric
t = turbulent

Novelty and Significance Statement

The novelty of the current work consists in the development of a theoretical model of fuel regression in the direction parallel to the oxidizer flow in an axial-injection-end-burning hybrid rocket. The model was essential in order to provide meaningful correlation laws for the regression rate from the main operational quantities, which have been obtained from experiments performed in a dedicated pressure-controlled combustion chamber. The model was validated by a comparative study using oxygen and nitrous oxide. In addition, a design methodology for fuel grain is illustrated with both oxidizers, highlighting the main design differences with classic hybrid rocket configurations. Finally, the effect of the nozzle on the axial component of the regression rate is shown.

Author Statement

Conceptualization, Methodology, Investigation, Data Curation, Writing - Review & Editing, Supervision, Project administration and Funding acquisition - G.G., M.F., S.S. and H.N.

1 Introduction

The benefits and drawbacks introduced by hybrid rocket engines are well known among the rocket society [1, 2]. Non-conventional configurations have been developed over the years to overcome the intrinsic issues of classic configuration [3]. In this scenario, the idea of the axial-injection end-burning hybrid rocket (AIEB) took hold at Hokkaido University with the aim of improving hybrid rocket technology [4].

A typical hybrid rocket configuration consists of a solid-phase tubular fuel and a liquid or gaseous oxidizer. Oxidizer passes through the grain port, and combustion occurs in the central hole in the boundary layer developed over the solid fuel surface. This configuration introduces some drawbacks, and the AIEB hybrid rocket was mainly proposed to fix two intrinsic issues: the OF shift occurring in long burning times firing tests and throttling operations, and low regression rates [5]. The former occurs because, depending on the specific configuration, the product of the regression rate and the solid surface exposed to the combustion changes during the burning time. This results in a loss of specific impulse and a consequent potential increase in residual propellant weight. The latter feature restricts hybrid rocket technologies to low thrust scale motors since the consumption rate of plastic fuels is intrinsically limited in the typical range of oxidizer mass fluxes.

Therefore, the regression rate is the main quantity deserving in-depth studies, which determines the total mass flow rate and overall oxidizer-to-fuel mixture ratio, which, for a given chamber pressure, controls the motor thrust and the ideal specific impulse. In classic configurations, the first hybrid combustion theory accounting for the main underlying phenomena involved in the burning of classical polymeric fuels was developed in 1963 by Marxman and Gilbert [6, 7] and it still remains the starting point of design calculations and experimental comparisons. Fuels typically burned in hybrid rockets are classical polymers, such as high-density polyethylene (HDPE), hydroxyl-terminated polybutadiene (HTPB), and polymethylmethacrylate (PMMA), or polymers with metal additives to improve the density impulse [8, 9, 10, 11,12]. The fuel regression of these polymers is determined by the ratio between the heat flux to the surface and the heat of phase change; thus, it is limited by the heat and mass transfer mechanisms occurring from the flame to the fuel wall. The result of this theory is that the distance of the diffusive flame from the solid surface is primarily related to the local mass flux. In particular, the regression rate grows with the oxidizer mass flux, which is actually the key design parameter.

On the other hand, the AIEB hybrid rocket uses a cylindrical fuel with an array of a large number of small ports running in the axial direction, through which the oxidizer flows. A diffusive combustion flame takes place at each port exit. Neighboring ports may eventually merge because of their enlargement during the burning time, as shown in Fig. 1. In this configuration, the regression rate is composed of a radial and an axial component with respect to the flow direction. The radial component is related to the local mass flux in analogy with conventional hybrid rockets, while the axial one is related to the distance of the edge-flame from the grain surface. The latter is promoted by arranging numerous micro-ports evenly across the fuel surface and satisfies more than approximately 95% effective density/volumetric loading. This requirement represented a technological limit for a long time, which was overcome with the advent of 3D printers [13].

Differently from the regression rate in the classic configuration, many studies devoted to the experimental characterization of the axial component of the regression rate in AIEB hybrid rockets revealed an opposite trend with the mass flux and a high sensitivity with the chamber pressure, suggesting that the feedback mechanism between the fuel pyrolysis and combustion is far from the above-mentioned theory [14,15,16]. Most of the research employed oxygen (O_2) or a mixture with nitrogen (N_2) as an oxidizer [17,18,19,20]. Also, recent studies have introduced nitrous oxide (N_2O), which is ideal for kick motors working in deep-space exploration applications because of its low toxicity and self-pressurization features [21]. For these reasons, N_2O, in addition to O_2, was adopted as the oxidizer in this study. Many empirical correlations have been explored in the past for different oxidizers and geometrical configurations; however, an explanatory theory has never been developed. In this scenario, the need for a phenomenological analysis arose in order to deeply understand the combustion physics of the problem and improve the empirical regression laws by involving physical parameters suggested by the theoretical analysis. Thus, the purpose of this study is to establish a novel model for the regression in AIEB hybrid rockets supported by experimental results obtained with gaseous oxygen and nitrous oxide in a range of chamber pressure between 0.1 and 3.0 MPa and mass fluxes between 20 and 1000 kg/m^{2}s at different port diameters included between 0.5 and 3 mm. The proposed phenomenological correlations have been further validated by firing tests of complete AIEB hybrid rockets, whose results confirmed the theoretical trends observed in the dedicated pressure-controlled tests.

The definition of a design methodology for the combustion chamber and multiport fuel grains is a further novelty of the work. In previous works, we intuitively demonstrated the benefits of introducing several ports for the reduction of unburnt fuel mass at the end of firing tests. In the last section of the paper, we have demonstrated by analytical analysis the effectiveness of using multiport geometries for the reduction of post-test fuel mass, which was highlighted by just experimental evidence in our previous works. In addition, the same procedure reveals the effect of the oxidizer choice on the motor geometry.

The work consists of three sections. Firstly, the experimental setup and the results of the study of the combustion characteristics of AIEB single-port fuel are shown. Visualizations of different operating conditions are displayed, and the main operative parameters affecting the regression rate are given. Secondly, phenomenological regression rate laws are developed, and the main differences introduced by using nitrous oxide with respect to oxygen are highlighted. Finally, a design methodology for the AIEB fuel grain design is illustrated, and additional experimental firing tests of the full AIEB configuration are shown.

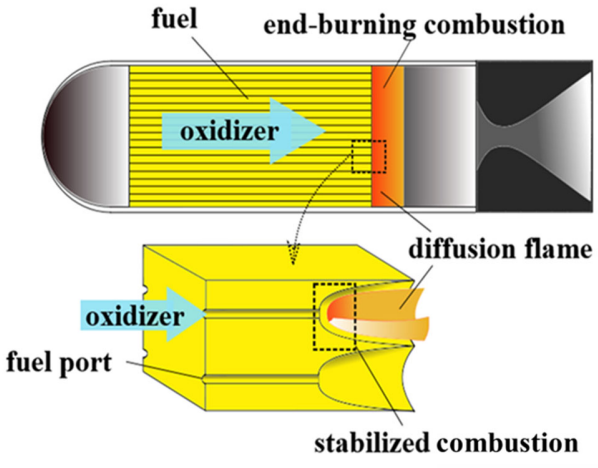

Fig. 1 Concept of an end-burning hybrid rocket motor [22].

2 Experimental Setup and Results

This section describes the facility and test apparatus employed for the evaluation of the regression rate in AIEB. Two experimental campaigns are shown, performed with two different oxidizers, i.e., gaseous oxygen and nitrous oxide. The data will be compared, highlighting the main combustion differences among the two oxidizers.

2.1 Experimental set-up

Although AIEB employs grain fuels featuring multiple small oxidizer ports, this study adopted a single-port PMMA fuel, displayed in Fig. 2, to reduce the uncertainty of the evaluation of the regression rate, which is the focus of the current work. The oxidizer ports have been manufactured by drilling PMMA square bars. The outer dimensions of the fuel grain are 20x20x30 mm.

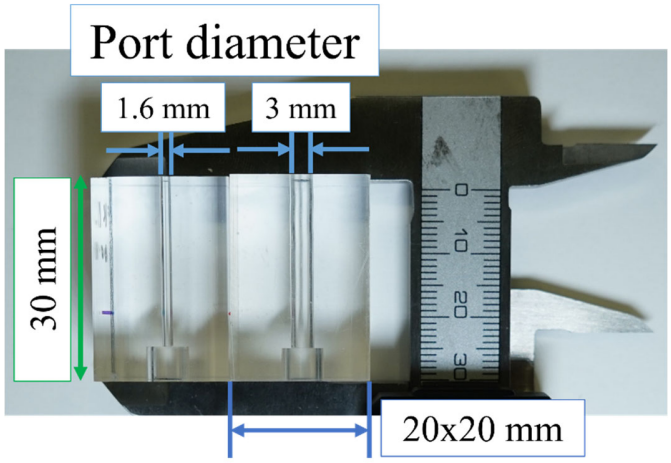

Fig. 2 PMMA fuel used in this study.

Fig. 3 shows the schematic of the experimental set-up employed in this study. Several sensors and recording devices were applied to the combustion chamber and supply lines. The detailed performance of these devices is shown in Table 1.

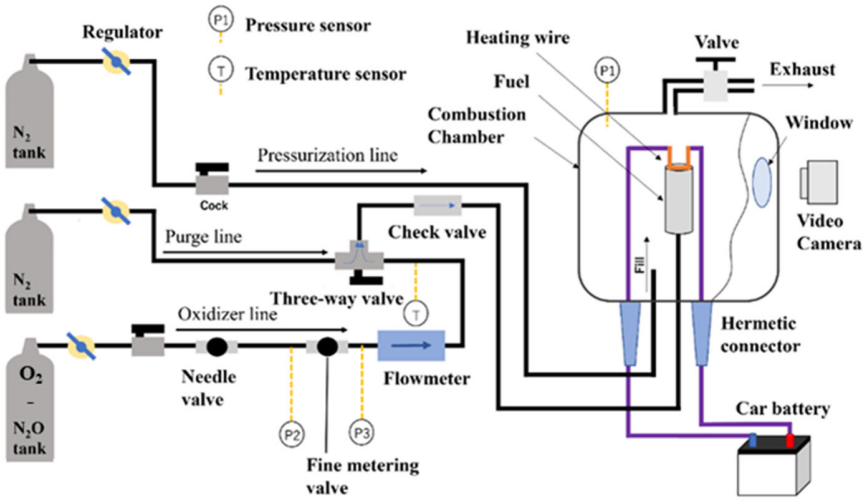

Fig. 3 Schematic of the experimental apparatus.

Table 1 Details of the sensors and devices.

Measuring device	Model	Range	Sensor error
Pressure Sensors	PHB-A-20MP (Kyowa Electronic Instruments)	0-20 MPa	±0.044 MPa
Type-K thernocouple	397-1258 (RS PRO)	-40/1100 C	±1.5 C
The oxidizer volumetric flow rate	SLA 5850S (Brooks Instrument)	0-50 NL/min	±0.9 %
Data logger	EDX-100A (Kyowa Electronic Instruments)		
Video camera	Sony		

The combustion chamber was equipped with two opposite round windows, as displayed in Fig. 4a. The first window is used for the fuel grain lighting by a 100 W work light, while the second one is for the video recording by a high-speed camera. The chamber is made of stainless steel to withstand the high pressures. The chamber is provided by two gas inlets close to the grain base, which are used for the oxidizer supply and chamber pressurization by pure nitrogen. Buoyancy effects are assumed to be negligible because the characteristic Reynolds number is typically over 10^4 in this application. For this reason, the fuel regression is assumed to be independent of the fuel orientation, and this was placed vertically inside the combustion chamber, as displayed in Fig. 4c. The connection and adhesion of the fuel grain with the oxidizer supply line are ensured by a high-temperature-resistant epoxy glue. Two outlets are placed upside the chamber for the exhaust of the combustion products and the adjustment of the pressure to the desired operating condition.

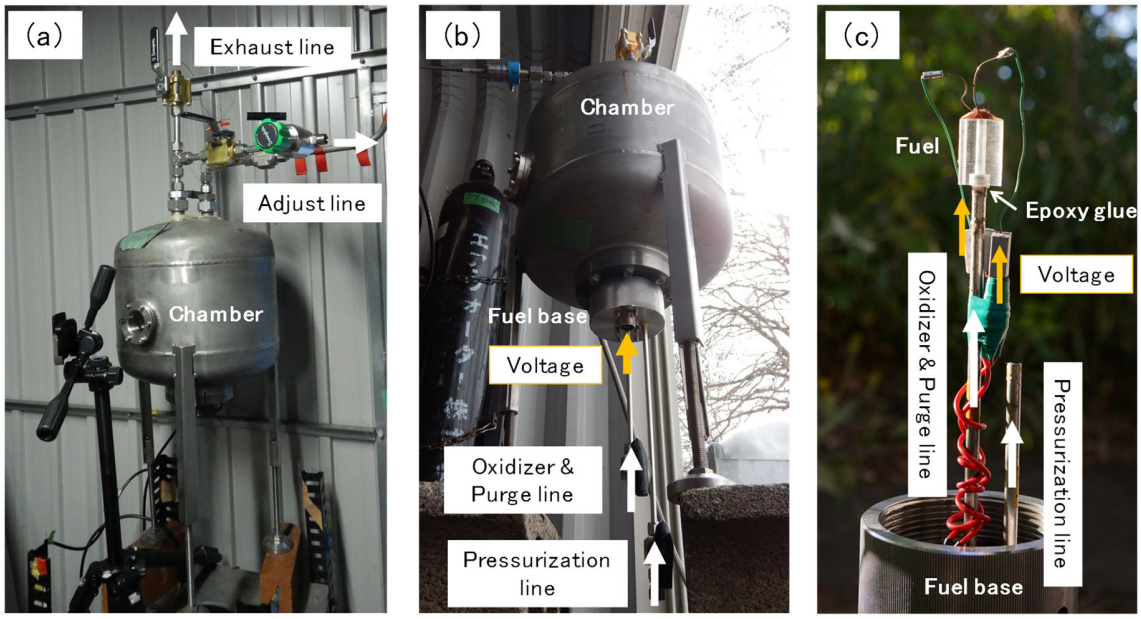

Fig. 4 Pressure chamber side view (a), lower view (b) and fuel base (c).

Because of the low amount of oxidizer mass flow rate injected in the port, a mass flow rate controller was used for the measurement, with the additional feature of adjusting the flow rate to a constant input value. When a steady operative condition in terms of chamber pressure and mass flow rate was achieved, the fuel ignition was triggered, supplying voltage to a nichrome wire placed at the top of the grain surface. The data logger and video recording were started simultaneously in order to synchronize the images with the recorded data. Finally, when the flame reached the fuel base, the fuel combustion was shut down by the purge line. Typical pressure and mass flow rate measurements recorded during the burning time are displayed in Fig. 5. Although the chamber pressure tends to increase due to the fuel combustion in the chamber, it is real-time controlled, achieving a steady-state operative condition.

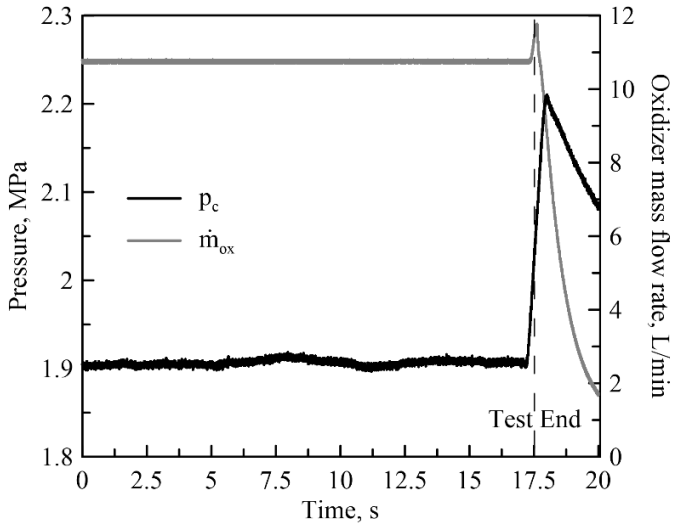

Fig. 5 Chamber pressure and mass flow rate measured during the burning time.

From the recorded movies, the flame tip positions were plotted as a function of time. Fuel regression rates were calculated from video using a flame tracker [23]. The regression rate was defined as the velocity at which the flame tip spreads upstream.

Experimental results were fitted to a line, and the regression rate was calculated by evaluating the slope of the linear trend line. An example is given in Fig. 6.

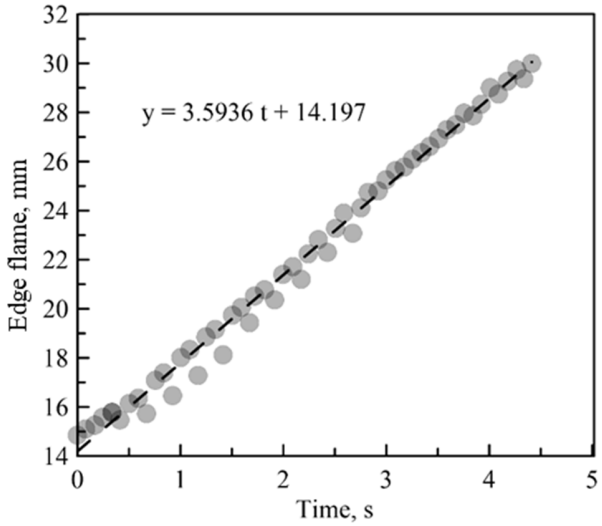

Fig. 6 Example of RGB flame tracker result (Oxygen, 0.52 MPa, 185 kg/m^{2}s).

2.2 Combustion Visualizations

The regression rate of the fuel grain is evaluated by combustion visualizations through the equipped chamber window. Fig. 7 displays the three typical operative conditions that can be experienced when firing an AIEB hybrid rocket by varying the oxidizer velocity (or mass flow rate), assuming constant chamber pressure. The regression mode is the desired working condition, in which the stability of the flame position on the top of the fuel grain is achieved. During the regression mode, the time derivative of the flame stand-off distance from the grain top, x^*, is close to zero in a moving reference frame with the axial fuel recession; thus, a characteristic flame stand-off distance can be recognized. The flame distance increases with the oxidizer velocity, leading to a reduction of the heat flux and fuel regression rate. Two limiting conditions are exhibited for low and high values of mass flow rates (or oxidizer velocities), which are flame-spread and blow-off, respectively. Both of these phenomenon concern the instability of the flame edge on the top of the fuel grain. In the former case, the time derivative of x^* is negative, indicating that the oxidizer speed is not high enough to sustain the flame on the top surface; the opposite occurs with blow-off. The visualizations of the three modes using oxygen are here described.

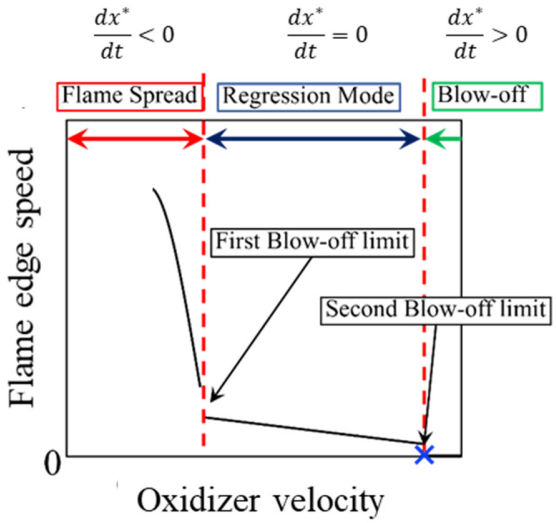

Fig. 7 Flame spread, regression and blow-off modes at different oxidizer velocity. x^* indicates the distance of the flame edge from the grain surface.

Fig. 8 displays the transient regression of the fuel grain during the burning time with a mass flow rate of 0.13 g/s, a chamber pressure of 0.1 MPa, and a port diameter of 3 mm. The combustion is triggered by an electrically loaded nichrome wire applied at the surface of the grain end. The nichrome wire produces high temperatures, which promote combustion when the oxidizer is injected into the grain port. In the next few seconds, an axisymmetric diffusion flame takes place on the edge of the central hole. While the gap between the fuel grain and the diffusion flame is clearly visible in the radial direction, this is not noticeable along the axial one. In the same way, the fuel grain is consumed in two directions by different burning rates; in particular, the axial component, $\dot{r}_{\parallel}$, is usually higher than the radial one, $\dot{r}_{\perp}$. For this reason, differently from a classic configuration, the burning time is defined by the grain length rather than the radial thickness. In this particular case, the flame took 29 seconds to reach the fuel base, and a large amount of fuel remained unburnt in the radial direction. The design criteria aimed at optimizing the fuel shape and size are described in the last section of the current work.

(a) t = 0 s.

(b) t = 6 s.

(b) t = 15 s.

(c) t = 23 s.

(d) t = 29 s.

(e) t = 30 s.

Fig. 8 Snapshots of the fuel regression during the burning time.

The sensitivity of the regression rate from the motor operative conditions is higher in the AIEB configuration than in the classic one. In the latter, the regression rate is the result of a diffusion-limited flame, and it usually varies in a narrow range between 0.2 and 1 mm/s by increasing the port mass flux; on the other hand, the regression rate in AIEB is the result of the heat transferred from the mixing-kinetic-limited flame edge, and it could vary between 0.3 and 10 mm/s by slightly changing the chamber pressure and the oxidizer mass flow rate. The large increase in the axial component of the regression rate is usually observed when the flame spread condition is achieved. In this case, the flame slips into the grain port, and a large amount of fuel may remain unburnt at the end of the firing test. Fig. 9 displays a firing test performed with a mass flow rate of 0.11 g/s, a chamber pressure of 0.1 MPa, and a port diameter of 3 mm, in which the flame spread occurred. As shown, the flame edge reaches the fuel base in 5 s by decreasing the mass flow rate to only 0.02 g/s. Therefore, the transition from the regression mode to the flame spread is clearly defined by a sharp border.

(a) t = 0 s.

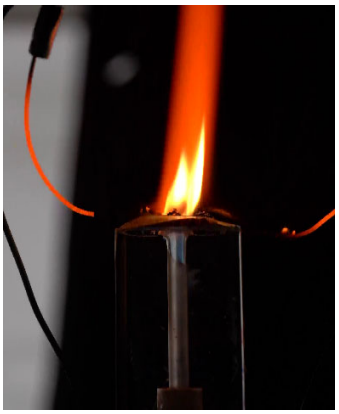

(b) t = 1 s.

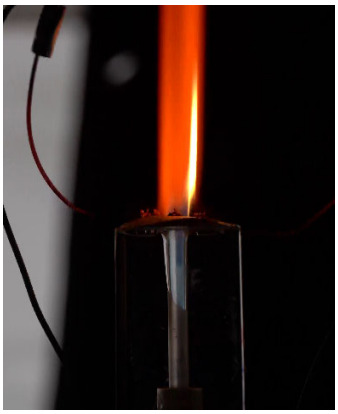

(c) t = 2 s.

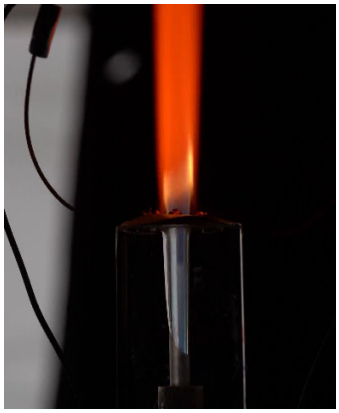

(d) t = 3 s.

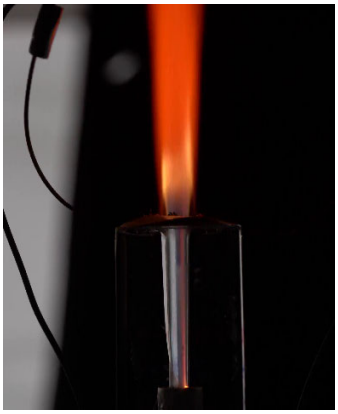

(e) t = 4 s.

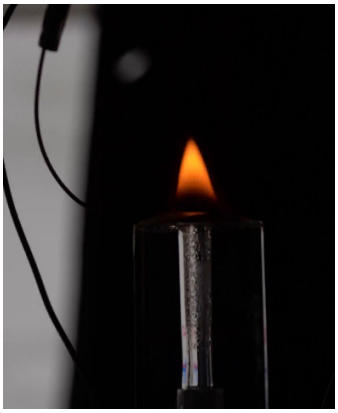

(d) t = 5 s.

Fig. 9 Snapshots of the flame spread during the burning time.

Finally, Fig. 10 displays a series of snapshots of a firing test near the blow-off limit. The firing test has been performed with a mass flow rate of 0.7 g/s, a chamber pressure of 0.1 MPa, and a port diameter of 3 mm. The firing test was shut down after around 2 minutes. Compared to the typical AIEB working condition, the radial component of the regression rate was larger than the axial one. The mixture ratio is extremely oxidizer-rich, resulting in a high-luminance flame. For larger mass flow rates, no flame is established at the top of the grain surface.

In this scenario, this work only concerns the regression mode. Phenomenological regression rate laws have been developed to obtain the correct modelling of the flame stand-off distance, which is the key quantity for the evaluation of the regression rate.

(a) t = 0 s.

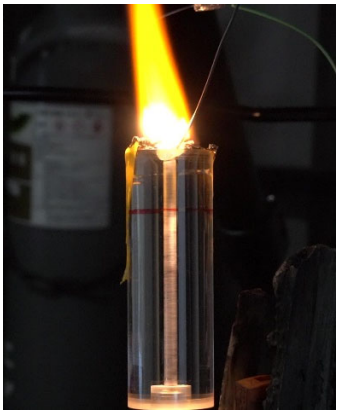

(b) t = 25 s.

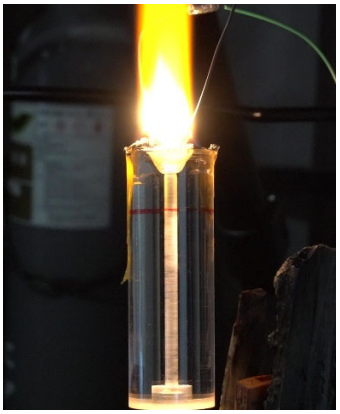

(c) t = 50 s.

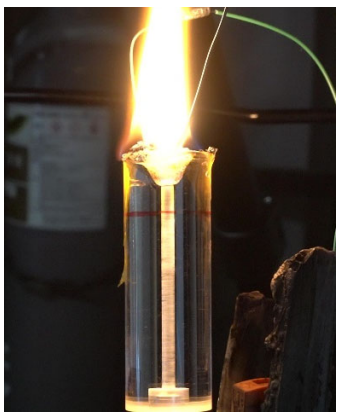

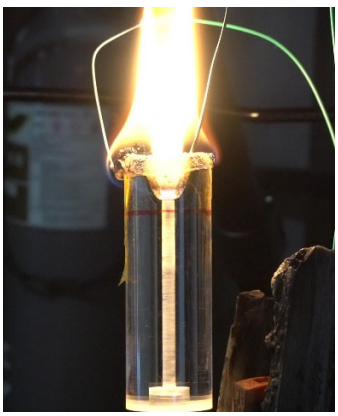

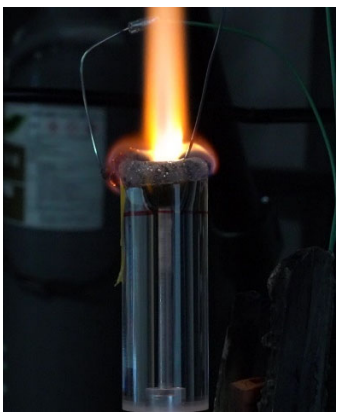

(d) t = 75 s. **(e) t = 100 s.** **(d) t = 120 s.**

Fig. 10 Snapshots of a firing test near the blow-off.

2.3 Experimental Results

The results of two different experimental campaigns with gaseous oxygen and nitrous oxide are shown in this subsection, with a total of 58 tests performed in different operative conditions in terms of pressure, mass flow rate, and port diameter, which are respectively included between 0.1 and 3.39 MPa, 0.03 and 1.69 g/s, 0.5 and 3 mm for the oxygen, and 0.4 and 2.01 MPa, 0.033 and 0.437 g/s, 0.8 and 3 mm for the nitrous oxide. The operative conditions and the parallel component of the fuel regression rate to the oxidizer flow are summarized in Table A.1 in Appendix A. The trends of the axial regression rate with the main parameters are evaluated by observing the exponents of the following linear regression trends:

$$\dot{r} = a\, \dot{m}_{ox}^{b}\, p_c^{c}\, D_p^{d} \tag{1}$$

The coefficients are summed up in Table 2. Note that coefficient a returns the regression rate in mm/s giving in input $\dot{m}_{ox}$ in kg/s, p_c in MPa and D_p in millimetres. The quality of the regression laws can be appreciated in Fig. 11, which $\dot{r}_{\parallel} / \dot{m}_{ox}^{b} D_p^{d}$ versus the chamber pressure.

Table 2 Linear regression parameter of Eq. (1).

Oxidizer	a	b	c	d	R^2
O_2	0.081	−0.51	1.48	1.12	0.99
N_2O	0.0083	−0.56	1.86	1.27	0.99

As an overall result, the regression rate increases with chamber pressure and port diameter, while it decreases with mass flow rate. Note that this trend is totally opposite of the regression rate in classic hybrid rockets, in which it increases with the oxidizer mass flux that is the main parameter, affecting the distance of the diffusion flame from the grain internal surface; consequently, the regression rate increases with the mass flow rate and decreases with the port diameter. In addition, the exponent of the pressure is close to zero, except in limiting conditions where radiation or chemical kinetic effects become dominant [24].

Essential information has been acquired for a deep understanding of the combustion phenomenology developed on the top grain surface. In particular, it can be observed that the exponent of the mass flow rate mostly remained constant among the two oxidizers, while that of the chamber pressure increased from 1.48 in the case of oxygen to 1.86 with nitrous oxide. Fig. 12 displays the comparison of the regression rate with the chamber pressure in the range of 0.1 and 2.0 MPa for nitrous oxide and oxygen. As shown, the regression rate varies from around 1 to 10 mm/s for oxygen and from 0.1 to 2.5 mm/s for nitrous oxide. This comparison suggests that the amount of heat flux transferred from the flame to the grain surface is higher when using O_2. These results are not obvious; indeed, the regression rate obtained with N_2O in classic hybrid rockets is comparable to or even higher than O_2 [25]. In addition, the flame spread easily occurs with oxygen, while the blow-off can be observed only in paradoxical operative conditions. The opposite trend is observed with nitrous oxide.

Note that the quantities involved in Eq. (1) are significant from a statistical point of view since they are statistically independent, but not from a physical point of view. Therefore, they should be rearranged in terms of the theoretical quantities in order to give a reasonable explanation regarding the observations previously cited.

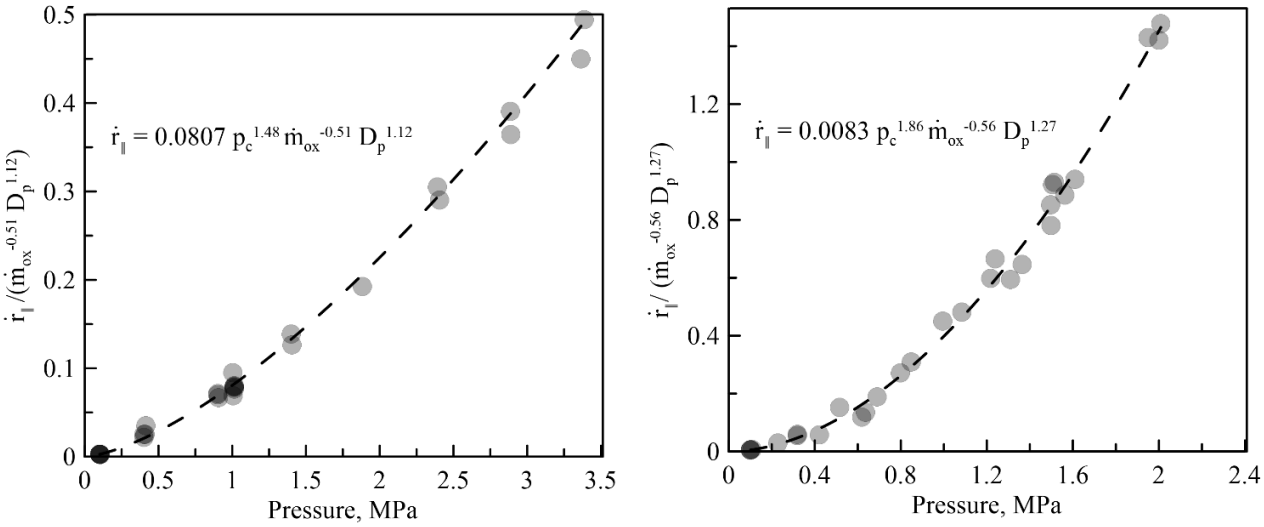

(a) Oxygen. **(b) Nitrous oxide.**

Fig. 11 $\dot{r}/\dot{m}_{ox}^{b}D_p^{d}$ versus the chamber pressure (the darker the circle, the greater the repeatability).

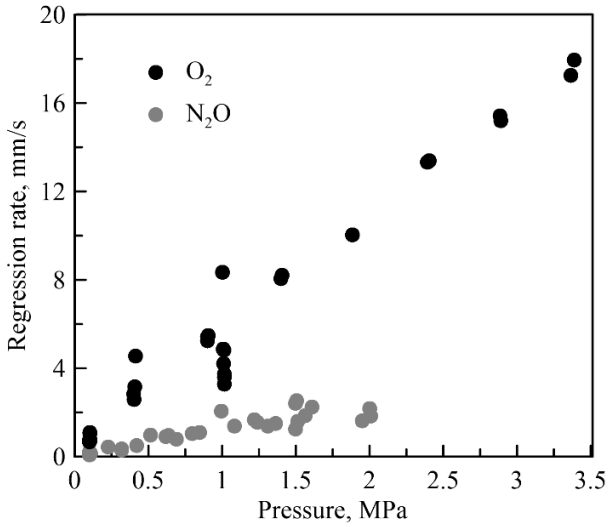

Fig. 12 Regression rate with the chamber pressure (O_2 vs N_2O).

3 Regression Rate Model

In this section, a regression rate model is developed in order to elucidate the combustion mechanisms developed in the combustion chamber and identify the key parameters affecting the regression rate. The model was adapted to the different oxidizers, highlighting the main differences and the higher sensitivity of the regression rate to pressure in the case of nitrous oxide.

3.1 Physical model description

The combustion visualizations displayed in subsection 2.2 are schematized in Fig. 13 for the different oxidizers. Fig. 13a displays the combustion mechanism of gaseous oxygen with gasified fuel. As mentioned above, the regression rate is composed of two components. The radial component is fed by the energy developed by the diffusion flame, and it depends on the distance between the diffusion flame and the lateral exposed surface. From the work of Marxman et al. [6], this component is primarily dependent on the local mass flux, or, for the sake of simplicity, it can be modelled like $\dot{r}_\perp = a_\perp G_{ox}^{n_\perp}$. The component parallel to the gas flow requires a different treatment. When the oxidizer gets close to the top of the grain, it mixes with the fuel, and it is heated by the flame reaching the optimum combustion conditions in a characteristic space, the so-called flame stand-off distance, which is indicated in this work with x_p for oxygen. At this location, the edge-flame takes place, from which the diffusion flame is developed. Therefore, the parallel component of the regression rate is dependent on the distance of the edge-flame from the fuel surface.

The combustion mechanism is slightly different when nitrous oxide is used as an oxidizer. Indeed, differently from the previous case, the dissociation of nitrous oxide occurs before fuel and oxygen combustion. As shown in Fig. 13b, the combustion mechanism can be summed up in the following steps:

1. Firstly, the nitrous oxide is exothermically dissociated in nitrogen and oxygen, increasing the temperature of the mixture in the characteristic space indicated as x_d. For the sake of simplicity, the zone in which the decomposition occurs is schematized as a thin flame.
2. Secondly, the hot oxygen burns with the fuel, developing the edge-flame in an additional space x_p (the same notation highlights the parallelism with the oxygen case).
3. Then, the diffusion flame takes place, originating from the edge-flame.

Therefore, the stand-off distance of the decomposition front, x_d plays a key role in the modelling of the regression rate, which is clarified by the mathematical model illustrated in the next section.

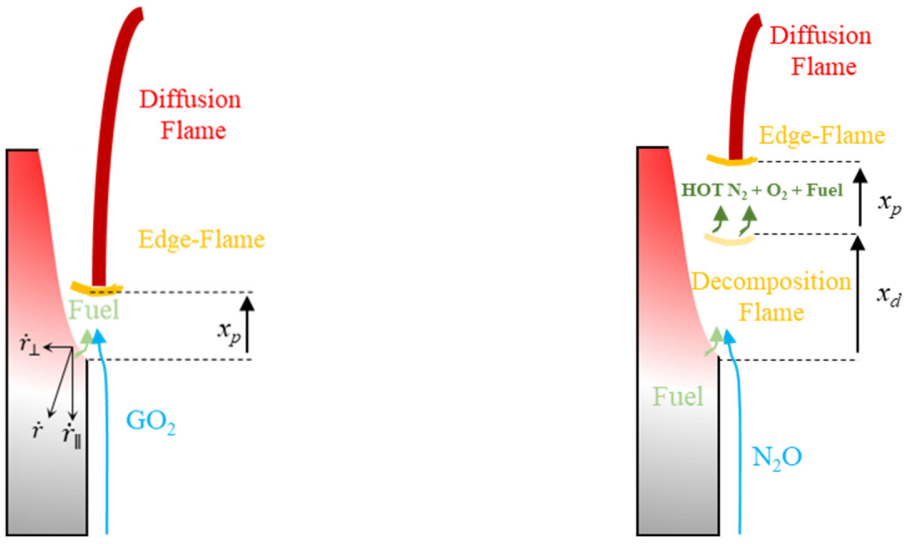

(a) O_2 with Fuel. **(b) N_2O with Fuel.**

Fig. 13 Axisymmetric sketch of the AIEB flame with oxygen and nitrous oxide.

3.2 Mass continuity and energy balance equation

The regression rate in AIEB is composed by two components:

$$\dot{\boldsymbol{r}} = \dot{\boldsymbol{r}}_{\parallel} + \dot{\boldsymbol{r}}_{\perp} \tag{2}$$

Where the bold quantities are vectors. Assuming that the two components are independent, for the sake of simplicity, the radial one is neglected in this section. In the case of pyrolyzing fuels, since no material is removed from the surface in a condensed phase (neither solid, such as in the case of fuel loaded with metal particles, nor liquid, as in the case of paraffin wax analysed later), the mass conservation at the gas-solid interface imposes that

$$(\rho v)_s = \rho_s \dot{r}_{\parallel} \tag{3}$$

Where ρ is the gas density at the wall, and v is the normal-to-wall velocity component due to the pyrolysis products injection; ρ_s is the solid fuel density and $\dot{r}$ is the local regression rate.

The energy balance at the gas-solid interface, taking into account the convective heat transfer from the gas to the fuel surface, the steady heat conduction into the solid and neglecting the radiative contribution, leads to the following relationship between the convective heat flux to the wall, $\dot{q}_w$, and the regression rate [26,27,28]:

$$\begin{aligned} \rho_s \dot{r}_{\parallel} \left[c_{ps}(T_s - T_a) + H_v \right] &= \dot{q}_w \\ \dot{q}_w &= \lambda_g \left. \frac{\partial T}{\partial n} \right|_{n=0} + \dot{q}_r \end{aligned} \tag{4}$$

Where $\dot{q}_r$ is the radiative component, n is the coordinate normal to the surface oriented from solid to gas, ρ_s is the density of the solid grain, c_{ps} is the specific heat of the solid grain, T_s is the surface temperature, T_a is the ambient temperature, H_v is the heat of pyrolysis, λ_g is the gas thermal conductivity, and $\left. \frac{\partial T}{\partial n} \right|_{n=0}$ is the temperature gradient at the wall included in the convective heat transfer term. The term in brackets at the left-hand side represents the effective heat of gasification of the fuel, which, further than the heat of pyrolysis, accounts for the heat radially conducted into the solid grain and absorbed by the oxidizer before the combustion with the gasified fuel. Note that Eq. (4), by properly defining the heat of pyrolysis, implicitly takes into account the heat transfer to the wall by the species diffusion [29]. Because the development of the edge-flame at the port outlet is a kinetic-limited phenomenon (especially with forced convection), the radiative heat flux is not considered in this work.

The fuel pyrolysis is, finally, modelled with the following Arrhenius-type equation:

$$\dot{r}_{\parallel} = A_s \cdot \exp\left(-\frac{E_a}{R T_s}\right) \tag{5}$$

Where A_s is the pre-exponential factor, E_a is the activation energy and R is the universal gas constant. The values of the constants appearing in Eqs. (4) and (5) considered for the PMMA fuel grains analysed in this work are summarized in Table 3.

Table 3 PMMA fuel properties and rate constants [30].

Density, ρ_s, kg/m^3	Specific heat, c_{ps}, J/kg K	Heat of pyrolysis, H_v, MJ/kg	Initial fuel temperature, T_a, K	Pre-exponential factor, A_s, mm/s	Activation Energy, E_a, kJ/mol
1150	$1200 + 8.57(\mathrm{T} - 273)$, $\mathrm{T} \leq 403$ K $2400, \mathrm{T} > 403$ K	1.55	300	$4.35 \cdot 10^7$	142

Next step is the postulation of the temperature profile. Assuming an exponential profile of the temperature in the space [28,31], the temperature profile is given by:

$$T(x) = Ae^{\frac{x}{x*}} + B \tag{6}$$

Where x^* is the distance between the solid grain and the flame front. Imposing that the temperature is equal to the surface temperature at $x = 0$, $T = T_s$, and equal to the flame temperature at $x = x^*$, $T = T_f$, the following relation is obtained:

$$T = T_s + \frac{(T_f - T_s)}{e - 1}\left(e^{\frac{x}{x*}} - 1\right) \tag{7}$$

Now, let us express the derivative at $x = 0$:

$$\left.\frac{\partial T}{\partial x}\right|_{x=0} = \frac{1}{x^*}\frac{(T_f - T_s)}{e - 1} \tag{8}$$

Finally, the regression rate can be defined as:

$$\dot{r}_{\parallel} = \frac{\lambda_g}{\rho_s\left[c_{ps}(T_s - T_a) + H_v\right]}\frac{(T_f - T_s)}{x^*(e - 1)} \tag{9}$$

Where Eq. (9) is coupled with Eq. (5) for the problem closure. Eq. (9) displays all the main dependencies of the regression rate from the combustion quantity and fuel properties. The relation of $\dot{r}_{\parallel}$ with the chamber pressure, mass flow rate and port diameter are taken into account in x^*. Therefore, a good modelling of x^* is required in order to achieve reliable regression laws of $\dot{r}_{\parallel}$ with the main propulsion parameters.

3.3 The case of the gaseous oxygen

The stand-off distance of the leap edge of the combustion flame from the grain surface is crucial for the modelling of the regression rate, as displayed in Eq. (9). In particular, we are interested in finding a phenomenological correlation that relates the regression rate (or stand-off distance), to the oxidizer mass flow rate, the port diameter, and the chamber pressure. In particular, the dependency of the regression rate on pressure is the most interesting feature because the exponent of the regression law displayed in Eq. (1) increased from 1.48 with oxygen to 1.86 with nitrous oxide. A first analytical modelling of the stand-off distance in laminar non-premixed mixing layers was mathematically expressed by Chung [31]:

$$\begin{gathered}\frac{\mu_{ox}/\rho_{ox}}{s_l}\frac{4}{D_p^2}x_p = \frac{\mu_s\rho_s}{8\mu_{st}\rho_{st}}\left[\frac{3^{Sc}}{1 + 2Sc}\frac{OF_{st} + 1}{OF_{st}}\right]^{\frac{1}{Sc-1}}\left(\frac{u_{ox}}{s_{l,st}}\right)^{\alpha} \\ \alpha = \frac{2Sc - 1}{Sc - 1}\end{gathered} \tag{10}$$

Where the subscripts ox and st refer to before and after burning conditions (assuming stoichiometric conditions), the subscript s refers to the grain surface conditions, $s_{l,st}$ is the laminar flame speed at stoichiometric condition, D_p the grain port diameter. Sc is a fictitious mixture Schmidt number, whose value should be found experimentally for any fuel/oxidizer couple. This approach was found to be valid in a very limited laminar cases, however, Eq. (10) is extremely useful to understand the main physical dependencies of x_p. Indeed, Eq. (10) can be re-arranged in:

$$x_p = K\left(OF_{st}, \frac{M_{w,st}}{M_{w,ox}}, \frac{T_{st}}{T_{ox}}, \frac{\mu_{st}}{\mu_{ox}}\right)\left(\frac{u_{ox}}{s_{l,st}}\right)^{\alpha} \tag{11}$$

Obviously, x_p increases with the oxidizer velocity and decreases with the laminar flame velocity by a constant which depends on the oxidizer condition, the gasified fuel properties and the port diameter. α is mainly correlated to the mixture

Schmidt number, therefore it is related to the mixing process of the oxygen in the fuel layer. Kalghatgi et al. proposed a generalization of Eq.(10) based on the definition of the flame Reynolds number defined as [32]:

$$Re_f = \frac{\rho_e s_{l,st} x_p}{\mu_e} \tag{12}$$

Which was mainly related to u_{ox}/s_l like Eq. (10), while ρ_e and μ_e are the density and viscosity at the port exit representing the gas condition between the port and the flame front. However, in hybrid rocket propulsion, the oxidizer velocity is strictly correlated to the chamber pressure, therefore the non-dimensional ratio $G_{ox}/\rho_{st} s_l$ was considered more appropriate in this kind of application. The previous approaches are based on the laminar flame speed, however the effect of the turbulence on x_p (or the flame Reynolds number) is not taken into account. In particular, the turbulence increases the flame speed reducing the stand-off distance. For these reasons, we proposed the following correlation:

$$Re_f = K \left(\frac{G_{ox}}{\rho_{st} s_{l,st}}\right)^{\alpha} \left(\frac{s_{l,st}}{s_{t,st}}\right)^{\beta} \tag{13}$$

Where $s_t/s_{l,st}$ represents the flame speed augmentation due to the turbulence. The next step is to highlight the dependency of Eq. (13) on the pressure, which lies in ρ by the ideal gas law, $s_{l,st}$ and the ratio $s_{t,st}/s_{l,st}$. Firstly, the laminar flame speed is given by the following theoretical relation:

$$s_l \sim p^{\frac{n}{2}-1} \left[\frac{\lambda_m}{c_{pm}} e^{-\frac{T_a}{T_f}}\right]^{1/2} \tag{14}$$

Where λ_m and c_{pm} are the mixture thermal conductivity and specific heat, T_a is the combustion activation temperature and n is the reaction order of the specific fuel/oxidizer couple, which is assumed to be close to 1.75 [33]. An additional effect of the pressure on the ratio $s_{t,st}/s_{l,st}$ was found in Ref.[34,35]; in particular, the turbulent flame speed increases with respect the laminar one increasing the pressure and the Reynolds number. Rearranging Eq. (13), the expression that relates x_p with the oxidizer mass flow rate, the chamber pressure and the port diameter in terms of G_{ox} and Re is given by:

$$x_p = K_{O_2} \left(K, \frac{1}{e^{-T_{a/T_f}}}\right) \frac{G_{ox}^{\alpha}}{p^{\frac{n}{2}(\alpha+1)+\beta} Re^{\beta}} \tag{15}$$

Eq. (15) shows that the flame stand-off distance increases with the oxidizer mass flux and decreases with the Reynolds number. $e^{-T_{a/T_f}}$ of Eq. (14) was included in the constant K_{O_2} meaning that the stand-off distance decreases with quick chemical reactions. Four phenomena contribute to the effect of the pressure on x_p: the mass diffusion (included in α), the kinetic reaction and thermal diffusivity (obtained from the exponent $n/2-1$ in Eq. (14)), and the turbulence (included in β). Evaluating again α and β in Eq. (15) in our experiments, we found $\alpha = 0.61$ and $\beta = 0.10$. Using these values and $n = 1.75$ for the evaluation of the pressure exponent, we found that:

$$\frac{n}{2}(\alpha+1) + \beta \cong 1.50 \tag{16}$$

Which is close to the experimental pressure exponent displayed in Table 2. Eq. (5), Eq. (9) and Eq. (15) have been coupled to estimate the fuel surface temperature and the order of magnitude of the stand-off flame distance. The presence of a diluting gas, N_2, was neglected in the evaluation of the flame temperature, which has been calculated by chemical equilibrium, setting MMA ($C_5H_8O_2$) as fuel with a formation enthalpy equal to -348.7 kJ/mol [36]. The stoichiometric condition is found at $OF = 1.7$ with a flame temperature, $T_f = 3354$ K. The gas thermal conductivity and oxygen viscosity used in the calculation are 0.055 W/mK and $1.16 \cdot 10^{-5}$ Pa·s, respectively. The constant *K* was calibrated in order to fit the experimental data shown in Fig. 11. Fig. 14 displays the surface temperature and stand-off distance by varying the chamber pressure assuming a port diameter

of 1 mm and $G_{ox} = 100\ kg/m^2s$. The surface temperature increases from around 369 to 408 K, x_p drops from $33 \cdot 10^{-7}$ to $3 \cdot 10^{-7}$ m and the regression rate grows from 1.5 to 14 mm/s by increasing the chamber pressure from 0.5 to 2 MPa.

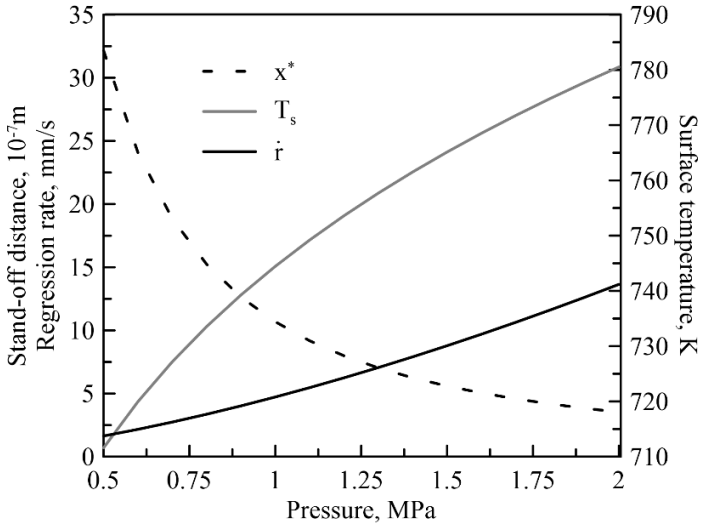

Fig. 14 Representation of surface temperature and stand-off distance vs. the chamber pressure with O_2.

3.4 The case of the gaseous nitrous oxide

The dissociation of N_2O should be included in the analysis for the modelling of the stand-off distance with nitrous oxide. Referring to the combustion schematic displayed in Fig. 13b, x_d, x_p and the interaction between the decomposition zone and combustion flame should be discussed. The distance between the fuel surface and decomposition flame can be modelled by a relation similar to Eq. (15) can be used:

$$x_d = K \frac{G_{ox}^{\alpha}}{p^{\frac{n_d}{2}(\alpha+1)+\beta} A_d e^{-T_{a,d}/T_d}} \cdot \frac{1}{R_e^{\beta}} \tag{17}$$

Where T_d is the decomposition flame temperature, A_d and $T_{a,d}$ are the pre-exponential constant and the activation temperature of the nitrous oxide decomposition [37]. n_d is the reaction order of the decomposition reaction of nitrous oxide, which is equal to 2 for chamber pressures below 40 atm, as displayed in Fig. 15 [38].

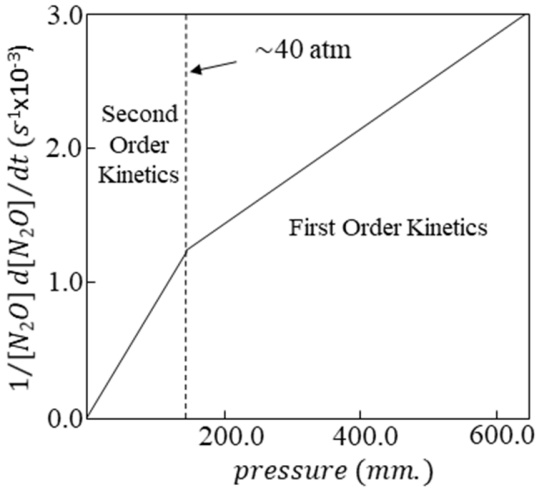

Fig. 15 Representation of the kinetic order of nitrous oxide decomposition with the working pressure [38].

Because the decomposition zone is heated by the combustion flame, the decomposition temperature is theoretically not coincident with the adiabatic value around 1907 K. Therefore, T_d is an unknown and an additional relation is required for the problem closure. Postulating the temperature profile like Eq. (6), the temperature between the surface grain and the decomposition flame, T_1, and the temperature between the decomposition and diffusive flame, T_2, are given by:

$$\begin{aligned} T_1 &= T_s + \frac{(T_d - T_s)}{e-1}\left(e^{\frac{x}{x_d}} - 1\right), \; x < x_d \\ T_2 &= T_d + \frac{(T_f - T_d)}{e-1}\left(e^{\frac{x-x_d}{x_p}} - 1\right), \quad x_d < x < x_p \end{aligned} \tag{18}$$

Imposing the heat flux continuity between the heat coming from the combustion flame and the heat released from the decomposition flame to the grain:

$$\left.\frac{\partial T_1}{\partial x}\right|_{x=x_d} = \left.\frac{\partial T_2}{\partial x}\right|_{x=x_d} \tag{19}$$

A relation for T_d is obtained, which is given by:

$$T_d = T_f \frac{x_d e}{x_p + x_d e} + T_s \frac{x_p}{x_p + x_d e} \tag{20}$$

When x_d is equal to 0, T_d coincides with the grain surface temperature, T_s; on the other hand, when x_p is equal to 0, T_d coincides with the diffusion flame temperature, T_f. Therefore, the decomposition temperature is dependent on the relative distance of the decomposition flame from the grain surface and the combustion flame. Because the N_2O is mostly heated along x_d and it quickly reacts with the fuel along x_p, x_d can be schematized as a pre-heat zone, while x_p as a thin reaction zone of a typical premixed flame structure (see Fig. 16). Therefore, it is reasonable to assume that $x_p/x_d \ll 1$ and the decomposition flame to be close to the combustion flame temperature, $T_d \approx T_f$.

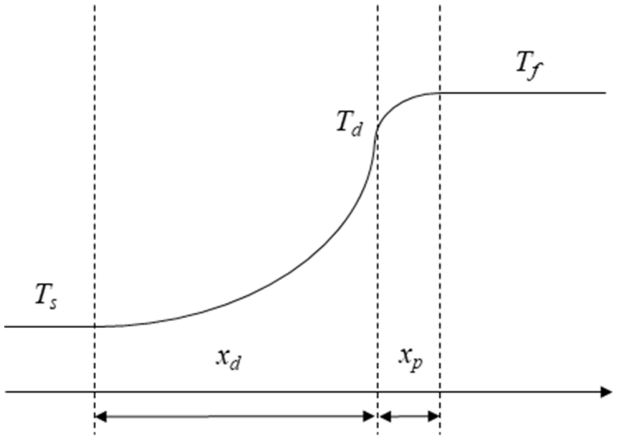

Fig. 16 Representation of the temperature profile from the grain surface to the flame temperature.

The above mentioned discussion allows us to consider constant $e^{-T_{a,N_2O}/T_d}$ in Eq. (17), which can be arranged in:

$$x_d = K_{N_2O} \frac{G_{ox}^{\alpha}}{p^{\frac{n_d}{2}(\alpha+1)+\beta} R_e^{\beta}} \tag{21}$$

Evaluating again α and β in Eq. (21) in our experiments, we found $\alpha = 0.69$ and $\beta = 0.15$. Using these values and $n_d = 2$ for the evaluation of the pressure exponent, we found that:

$$\frac{n_d}{2}(\alpha + 1) + \beta \cong 1.85 \tag{22}$$

Which is close to the experimental pressure exponent displayed in Table 2. The described model enables us to understand the physical reason for the pressure exponent growth with nitrous oxide. The increase in the sensitivity of the regression rate from the pressure is due to the increase in the reaction order from 1.75 to 2 of the decomposition mechanism occurring upstream of the combustion flame.

Eq. (5), Eq. (9), and Eq. (15) have been solved again to evaluate x_d and compare with x_p of the oxygen case. The stoichiometric condition is found at $\mathrm{OF} = 5$ with a flame temperature, $T_f = 3150$ K, while the same gas thermal conductivity and oxygen viscosity as in the previous subsection are set. A port diameter of 1 mm and $G_{ox} = 100\, kg/m^2 s$ have been imposed. The constant K_{N_2O} was calibrated to fit the experimental data of nitrous oxide. Comparing Fig. 17 with Fig. 14, x_d is roughly 7 times higher than x_p in the case of oxygen. Therefore, the combustion mechanism of nitrous oxide takes longer than that of oxygen. As suggested by the constant *K* of Eq. (15) and Eq. (21), indeed a longer distance is required by the nitrous oxide combustion than oxygen because the activation temperature of the N_2O thermal decomposition is $3 \cdot 10^4$ K [37], twice the activation temperature of the oxygen combustion with common hydrocarbons around $1.5 \cdot 10^4$ K [39]. Therefore, observing Eq. (14), a strong reduction of the laminar flame speed is expected in the case of N_2O. In addition, the diffusion of a larger amount of oxidizer is required with N_2O to achieve the stoichiometric condition, leading to a further extension of the flame stand-off distance. Consequently, the average surface temperature and regression rate are lower than in the oxygen case as well. Finally, the current analysis provides further information regarding the blow-off nature of AIEB. Often, the flame blow-off experimentally occurs at pressures close 0.4 - 0.5 MPa for nitrous oxide, assuming the mentioned G_{ox}. Observing Fig. 17, the stand-off distance is still below 10^{-4} m in this condition, which is largely below the near-blow-off flame distances of laminar flames (around 10^{-2} m) produced by non-premixed burners [31]. Therefore, this suggests that blow-off in AIEB is related to the excessive oxidizer-rich mixture due to the low regression rate rather than to the mixing process of oxidizer and fuel.

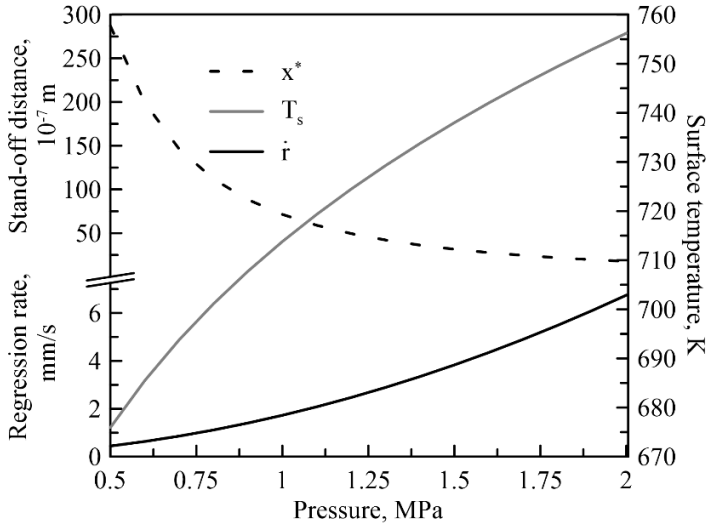

Fig. 17 Representation of surface temperature and stand-off distance vs. the chamber pressure with N_2O.

4 Axial Injection End-Burning Design Methodology

In this section, a design methodology for the AIEB fuel grain is given once the basic mission requirements are. The analysis shows how the motor dimensions change with the thrust scale, reducing the intrinsic mass losses of the AIEB configuration. Finally, firing tests of a full AIEB configuration are displayed and discussed.

4.1 Design methodology

Typical mission requirements are given in terms of total impulse, operative pressure and propulsion system volume. The total impulse, I, is given by:

$$I = T \cdot \Delta t$$
$$\dot{m}_{ox} = \frac{T}{\left(1 + \frac{1}{OF}\right) \cdot Isp} \tag{23}$$

Where T is the thrust, Δt is the burning time, $\dot{m}_{ox}$ is the oxidizer mass flow rate, and Isp is the specific impulse. Assuming to work at optimum condition, the OF, the specific impulse and the oxidizer mass flow rate are fixed. The fuel mass flow rate is defined by the surface exposed to the flame and the regression rate. The definition of the burning surface is hard to define in AIEB because the fuel grain consists of a series of ports with a diameter, d, center-to-center spaced from each other by a length, h (see Fig. 18). In this picture, ports are arranged on two circular crowns. The label, i, identifies the crown number, starting from the grain center.

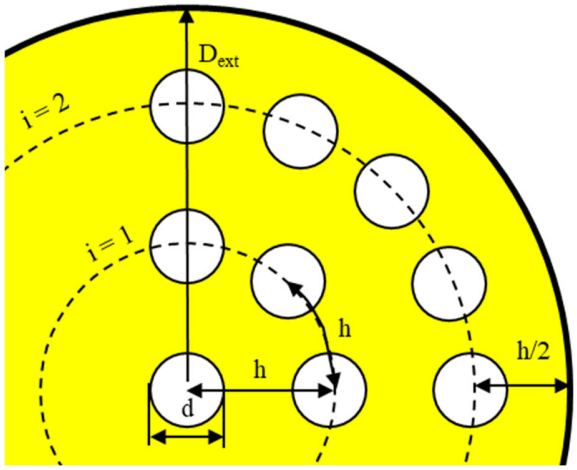

Fig. 18 Schematic of the oxidizer ports arrangement in EB.

The total area of the oxidizer ports, A_{ox}, and the equivalent total ports' diameter, D_p, can be calculated, giving in input a reasonable oxidizer mass flux:

$$A_{ox} = \frac{\dot{m}_{ox}}{G_{ox}}$$
$$D_p = \sqrt{4A_{ox}/\pi} \tag{24}$$

Note that the oxidizer mass flux in each port is equivalent to the total mass flux displayed in Eq. (24). Once known D_p, the axial regression rate can be evaluated by Eq. (1) and the external grain diameter, D_{ext}, is calculated as:

$$D_{ext} = \sqrt{\frac{4}{\pi}\left(\frac{\dot{m}_{ox}}{OF\rho_s\dot{r}_{\parallel}} + A_{ox}\right)} \tag{25}$$

Neglecting $\dot{r}_{\perp}$ and defining the fuel surface as the difference between the total and the oxidizer ports' area, the fuel mass flow rate, $\dot{m}_f$, and the total mixture ratio, OF, are given by:

$$\dot{m}_f = \rho_s\dot{r}_{\parallel}(\pi D_{ext}^2/4 - A_{ox})$$
$$OF = \dot{m}_{ox}/\dot{m}_f \tag{26}$$

Finally, the length of the fuel grain is computed by:

$$L_g = \dot{r}_{\parallel} \Delta t \tag{27}$$

The dimensions of the grain and the combustion chamber are given by Eq. (25) and Eq. (27). Differently from classic hybrid rockets, the number of ports is higher than 1. Fixing a number of ports, N_p, the diameter of the single port, d, is given by:

$$d = \sqrt{\frac{4A_{ox}}{\pi N_p}} \tag{28}$$

Because h is typically comparable to d, the radial component of the regression to the oxidizer flow, $\dot{r}_{\perp}$, cannot be neglected. As displayed in Fig. 19, the amount of unburnt fuel remaining at the end of the burning time is affected by $\dot{r}_{\perp}$ (Fig. 19a), which is usually lower than $\dot{r}_{\parallel}$, and the geometrical configuration of the ports (Fig. 19b). An additional fuel loss is also required in order to thermally shield the metallic case from the flames developed in most external ports. The mathematical expression of the unburnt fuel volume is not analytical due to the geometrical complexity; hence, an explicit formula cannot be obtained. However, it can be noted that the amount of unburnt fuel at the end of the firing increases when $\dot{r}_{\perp}$ is low compared to $\dot{r}_{\parallel}$ and h (see $\dot{r}_{\perp,1}$ in Fig. 19a); this operative condition is undesired and conceptually close to the flame-spread.

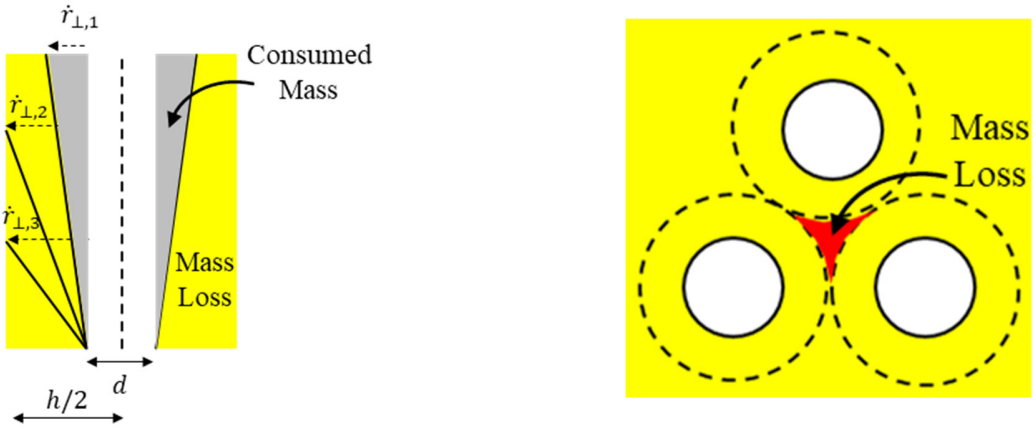

(a) **(b)**

Fig. 19 Fuel mass loss due to the geometrical configuration of the ports and the orthogonal component of the regression rate.

We can conclude that the total mass loss is related to:

$$m_{f,loss} \propto \left(\frac{\dot{r}_{\parallel}}{\dot{r}_{\perp}}\right)\frac{h-d}{2} \tag{29}$$

The objective of the AIEB design is to minimize $m_{f,loss}$. The optimization of the fuel configuration relies on the correct choice of h and d ratio, because the ratio $\dot{r}_{\perp}/\dot{r}_{\parallel}$ is mostly fixed by the operative conditions. Indeed, let us define a regression rate law of $\dot{r}_{\perp}$ as function of the oxidizer mass flux:

$$\dot{r}_{\perp} = a_{\perp}(G_{ox})^{n_{\perp}} \tag{30}$$

Where $a_\perp$ and $n_\perp$ are estimated by visualizations of the experiments as well, which are displayed in Fig. 20. For the sake of the simplicity, G_{ox} in Eq. (30) coincides with the oxidizer mass flux estimated at the beginning of the burning time.

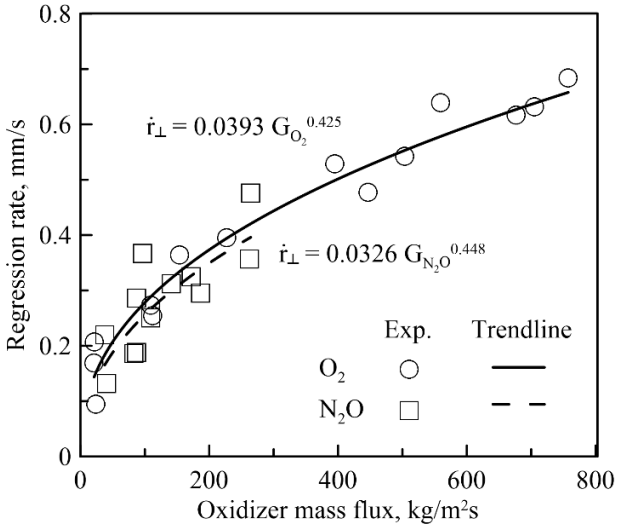

Fig. 20 Regression rate law of the perpendicular component to the grain axis with the oxidizer mass flux for oxygen and nitrous oxide.

The ratio $\dot{r}_\perp/\dot{r}_\parallel$ is given by:

$$\frac{\dot{r}_\perp}{\dot{r}_\parallel} = \frac{a_\perp}{a}\left(\frac{4}{\pi}\right)^{n_\perp} m_{ox}^{n_\perp - b}\, p_c^{-c} D_p^{-(2n_\perp + d)} \tag{31}$$

And the fuel grain length that remains unburnt at the end of the burning time, L_{ub}, is given by:

$$L_{ub} = \left[\frac{a_\perp}{a}\left(\frac{4}{\pi}\right)^{n_\perp} m_{ox}^{n_\perp - b}\, p_c^{-c} D_p^{-(2n_\perp + d)}\right] \cdot \left(\frac{h-d}{2}\right) \tag{32}$$

In this particular case, $n_\perp \approx b$, consequently the ratio of regression rate components is mostly insensitive to the mass flow rate, and decreases with the chamber pressure and port diameter. However, high chamber pressure and large ports' diameters are undesired design conditions. In AIEB hybrid rocket, L_{ub} can be further reduced by decreasing $h-d$, which can be accomplished by maximizing the number of ports. Note that, assuming a fixed external diameter, D_{ext}, the number of ports depends on the length of h and d. In particular, the following relation must return an integer number:

$$N_p = \sum_{i=1}^{n} \frac{\pi[D_{ext} - (2n + 1 - 2i)h]}{h} + 1$$
$$n = \frac{D_{ext} - h}{2h} \tag{33}$$

Where N_p is the number of ports, n is the total number of circular crowns (see Fig. 18), i is the circular crown number (i=1 and $i = n$ represent the most internal and external circular crowns). In this framework, the objective is to increase N_p by decreasing h as much as possible. The described procedure has been used by assuming the inputs displayed in Table 4 with oxygen and nitrous oxide. As displayed, assuming the same operative conditions, the combustion chamber of the oxygen case is characterized by a longer length and smaller diameter, while the opposite trend is observed using nitrous oxide. The schematic of the size of the grains obtained with the two oxidizers is displayed in Fig. 21.

Table 4 Example of mission requirements for the design of EB.

Input		Output	O_2	N_2O
Total impulse, I, $N \cdot s$	10000	Oxidizer mass flow rate, $\dot{m}_{ox}$, g/s	147.8	219.3
Thrust, T, N	500	Grain length, L_g, mm	469	72.2
Pressure, p_c, MPa	1.5	External Diameter, D_{ext}, mm	80.8	127.4
Mass flux, G_{ox}, $kg/s \cdot m^2$	100	Burning time, Δt, s	20	20
Port diameter, d, mm	5	Parallel regression rate, $\dot{r}_{\parallel}$, mm/s	23.5	3.60
		Perpendicular regression rate, $\dot{r}_{\perp}$, mm/s	0.27	0.26

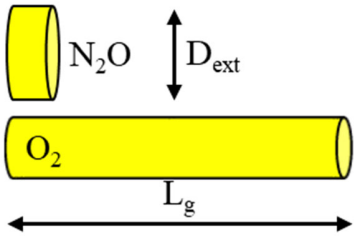

Fig. 21 Schematics of the grain dimensions with N_2O and O_2.

Assuming a port diameter of 5 mm, Fig. 22 displays the number of ports and the ratio between the unburnt and the total grain length, $\left(\frac{\dot{r}_{\parallel}}{\dot{r}_{\perp}}\right) h/L_g$, considering a geometrical configuration like that displayed in Fig. 18. Accordingly, the number of ports decreases from 1372 to 397 with oxygen and from 2306 to 687 with nitrous oxide by increasing h from 0.5 to 5 mm. N_p is higher for N_2O, because D_{ext} is 1.5 larger than the case of oxygen. On the other hand, the value of L_{ub} is larger with oxygen, because $\dot{r}_{\parallel}/\dot{r}_{\perp}$ of oxygen is around 7 times higher than nitrous oxide. However, the percentage of unburnt length compared to the grain length is mostly the same for both oxidizers. As shown in Fig. 22, the unburnt percentage increases from around 10% to around 90% in the same inter-port range.

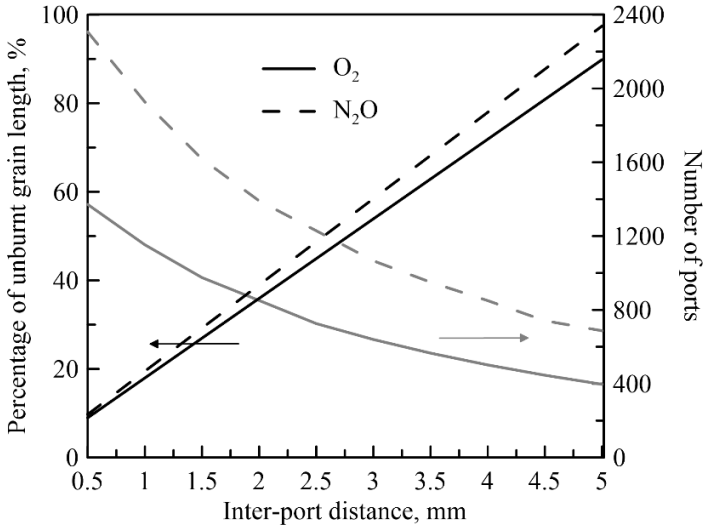

Fig. 22 Representation of the number of ports and L_{ub}/L_g with h.

Finally, we will show how the design changes by varying the motor thrust, considering the same total impulse of $10^4\ N \cdot s$. Fig. 23a displays that the burning time hyperbolically drops from 100 to 10 s, while the oxygen and nitrous oxide mass flow

rates linearly increase from 30 to 300 g/s and 44 to 489 g/s, respectively, by increasing the thrust level from 10 to 1000 N. Fig. 23b shows the grain length and the external diameter in the same thrust range. As shown, the grain length hyperbolically decreases from 2520 to 252 mm with oxygen and from 361 to 36 mm with nitrous oxide. On the other hand, the external diameter increases from 35 to 111 mm with oxygen and from 57 to 180 mm with nitrous oxide. Summing up, high thrust-level AIEBs require short and large fuel grains.

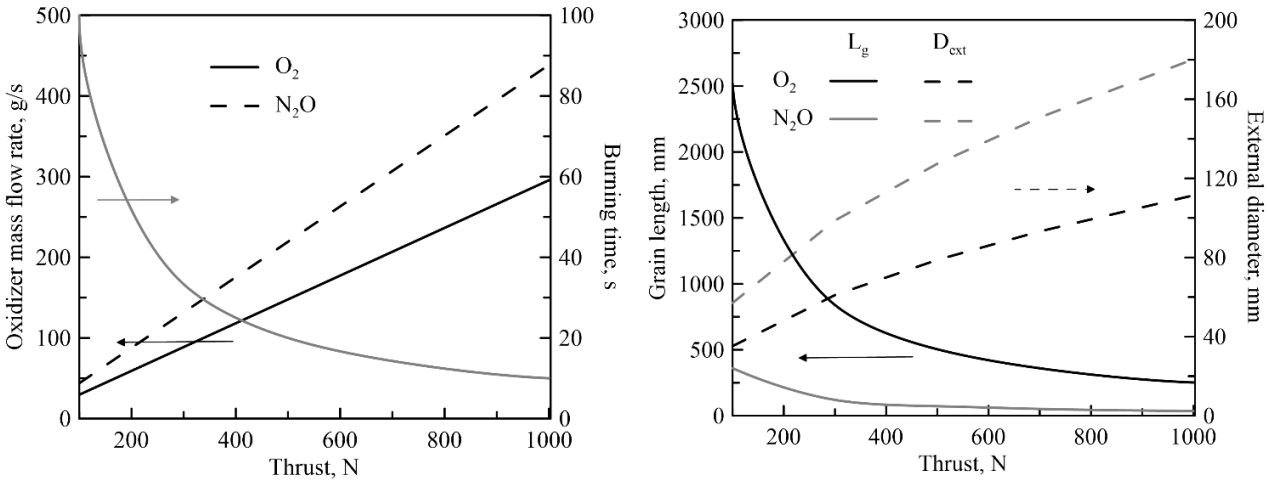

(a) Burning time and oxidizer mass flow rates.

(b) Motor length and external diameter in AIEB and classic configuration.

Fig. 23 Parametric analysis of the motor design with oxygen and nitrous oxide varying the thrust assuming a constant total impulse of 10^4 s.

Fig. 24 displays a comparison of the grain length and external diameter, considering AIEB and the classic configuration using O_2. Differently from the AIEB configuration, the grain length increases with the thrust from 190 to 602 mm, and the external diameter decreases from 168 to 76 mm. This simple analysis displays that the design criterion of AIEB is opposite to the classical hybrid rocket configuration. The regression rate characteristics of AIEB make this kind of motor more suitable for missions with high thrust levels than classic configurations, which are proper for low thrust scales, such as deep space missions.

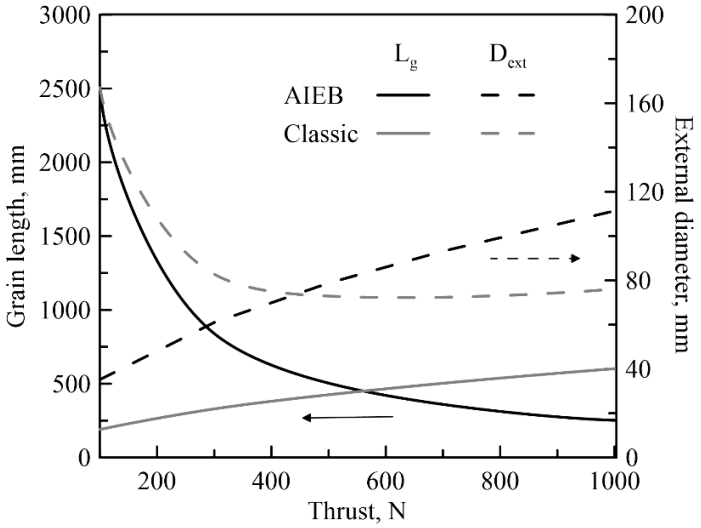

Fig. 24 Comparison of AIEB and classic configuration.

4.2 Experimental firing tests AIEB

Additional firing tests have been performed employing a full AIEB, whose schematic is displayed in Fig. 25a. Differently from the previous experiments, a graphite nozzle has been placed at the outlet of the combustion chamber. The fuel grain was manufactured by highly accurate 3D printers employing ultraviolet-curable resin consisting of 80 to 90% acrylic acid ester, 5% hexamethylene acrylate, and a photopolymerization initiator. The overall regression and combustion characteristics of the mentioned materials are close to those of PMMA. The fuel grain was accommodated into an optical window made of PMMA. The fuel-optical window assembly is displayed in Fig. 25b.

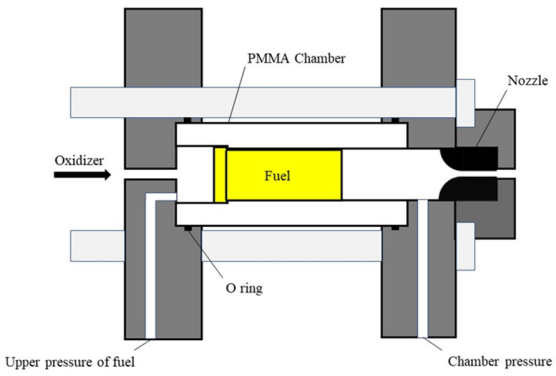

(a) Combustion chamber.

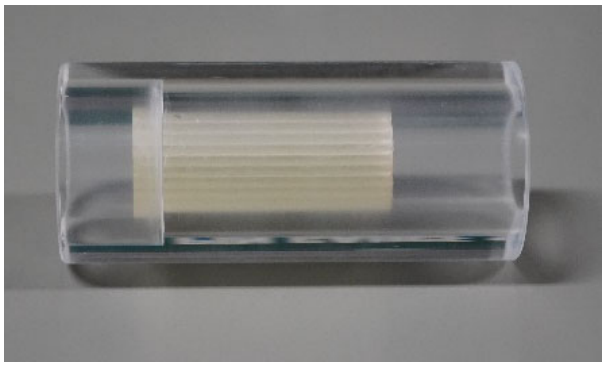

(b) PMMA external chamber and fuel grain.

Fig. 25 Schematic of the AIEB hybrid rocket firing test.

Note that the strict requirements of AIEB fuel grains in terms of accuracy and geometrical complexity can be currently satisfied only by involving 3D printers in the manufacturing process. Indeed, the development of AIEB was historically restrained by the technological evolution of advanced manufacturing methods, which were mainly restricted to the use of the drill. Such manufacturing methods limited the port density per unit of density area, leading to large amounts of unburnt fuel and strongly affecting the accuracy of the port diameters. The latter aspect is important for the combustion uniformity of the fuel top surface. Fig. 26 displays four examples of firing tests designed in order to investigate the combustion and regression

synchronization of the oxidizer ports at the end of the burning time. Fig. 26d is the most relevant, in which flame-spread occurred in two ports adjacent to the fuel accommodation case.

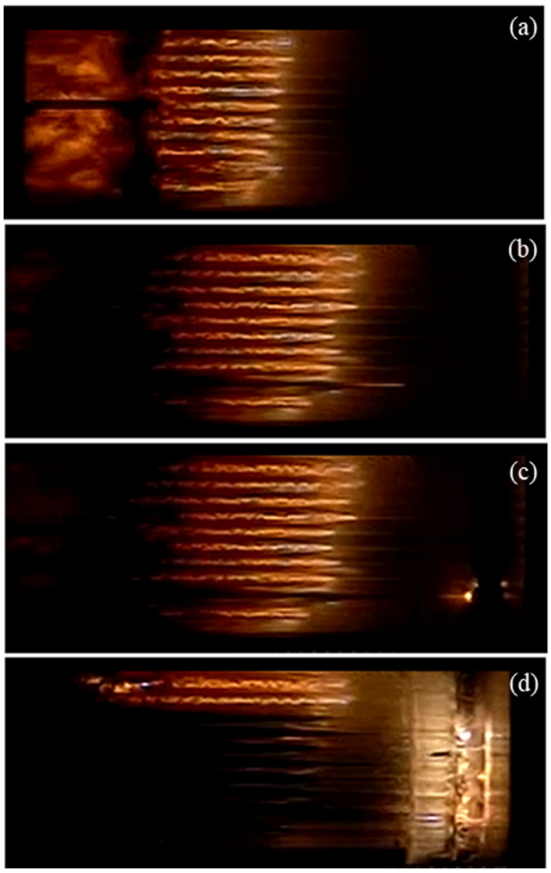

Fig. 26 Representations of non-uniform combustion due to the uncertainty related to the port manufacturing.

A series of experimental tests have been performed with gaseous oxygen by varying the injected mass flow rate from 1.43 to 1.88 mm/s. Consequently, the chamber pressure changed between 0.64 and 0.97 MPa. The fuel dimensions are displayed in Table 5. The recorded operative conditions are summed up in Table 6. Fig. 27 displays pictures of the fuel grain of a typical firing test at the end of the burning time.

Table 5 Dimensions of the fuel grain and nozzle.

External diameter, mm	20
Fuel length, mm	50
Port diameter, mm	0.3
Port Interval, mm	1.7
Number of ports	85
Nozzle throat diameter, mm	2.9

Table 6 Experimental firing tests.

Test	Mass flow rate, g/s	Chamber pressure, MPa	Regression rate, mm/s
1	1.43	0.64	3.47
2	1.48	0.64	3.43
3	1.72	0.83	4
4	1.8	0.89	4.31
5	1.83	0.97	4.31
6	1.88	0.75	4.5

(a) Lateral view. **(b) Front view.**

Fig. 27 A representation of the fuel grain after the firing test.

Table 6 displays that the regression rate increases with both pressure and mass flow rate. Indeed, the chamber pressure linearly increases with the oxidizer mass flow rate when the nozzle is employed. The current experimental campaign further highlights the need to perform dedicated experimental tests in pressure-controlled chambers to deeply understand the phenomenology of the regression rate and the role of the key parameters. Because $\dot{m}_{ox} \propto p_c$ and the port diameters are kept constant among the tests, Eq. (1) reduces to:

$$\dot{r} = a^* p_c^{b^*} \tag{34}$$

Which coincides with the formulation of the burn rate in solid rocket motors. From the results obtained in Section 3, the value of b^* should coincide with the sum of the exponents b and c of Eq. (1) around 0.97 for oxygen and 1.30 for nitrous oxide. Therefore, a linear trend of the regression rate with the chamber pressure is expected, which is highlighted in Fig. 28 showing the regression rate with the chamber pressure of the tests listed in Table 6. The linear trend was further confirmed by the extensive experimental campaign carried out with oxygen in our previous work [15]. Regarding nitrous oxide, a

pressure exponent of 1.30 was obtained in our previous experimental campaign [16], which is completely in line with our current work.

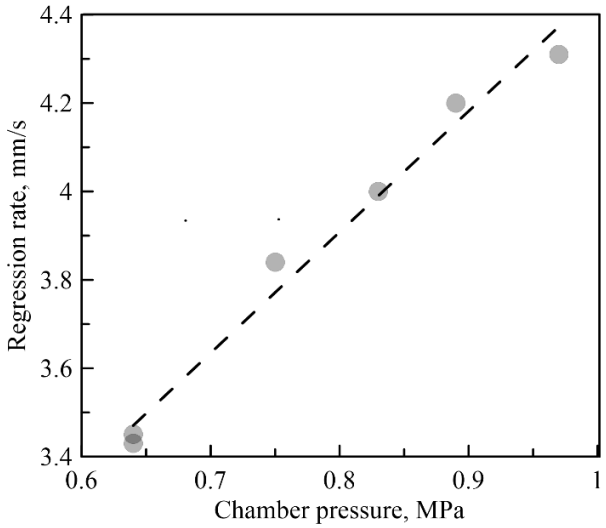

Fig. 28 Regression rate versus chamber pressure in AIEB firing tests.

Note that a pressure exponent close to 1 theoretically represents a limiting condition for the dynamic stability of AIEB and solid rocket motors [40]. Indeed, values of b^* lower than 1 ensure a constant chamber pressure and regression rate during the burning time, while higher values lead to a continuous increase in these quantities. Consequently, the intrinsic instability of AIEB is mitigated by the nozzle, which reduces the sensitivity of the regression rate on pressure from 1.48 to 0.97. Fig. 29a displays the chamber pressure and the oxidizer mass flow rate during the burning time in Test 1. As expected, the oxidizer mass flow rate and the chamber pressure were approximately constant after a long ignition transient of around 6 seconds. On the other hand, although a pressure exponent over one is observed with nitrous oxide, the pressure growth observed during the burning time in Fig. 29b is not dramatic. In this particular test, it increased from 0.45 to 0.57 MPa with a consequent increase in the regression rate and reduction of the average mixture ratio of around 7%.

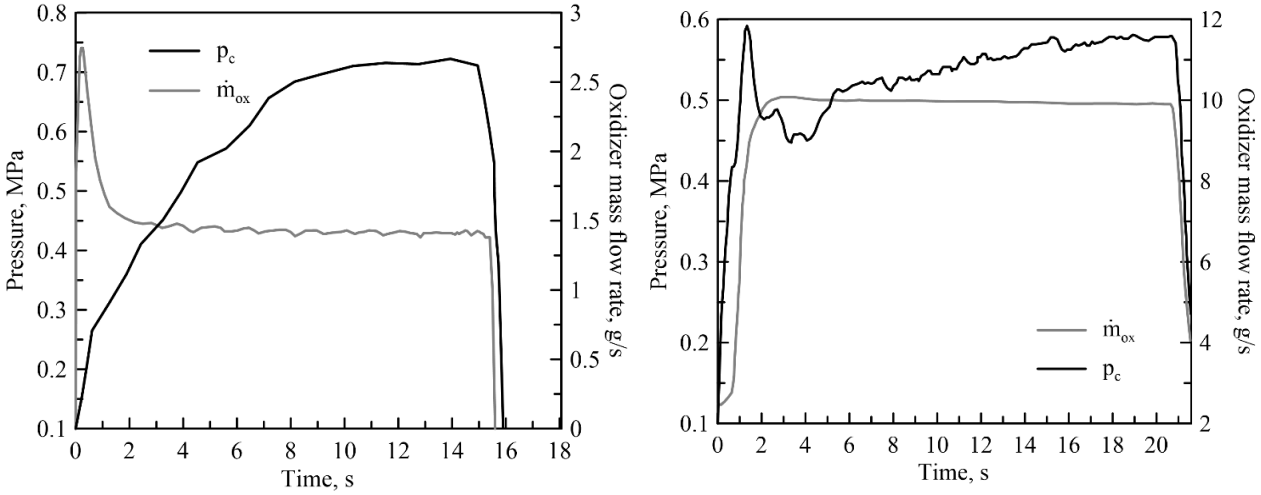

(a) Oxygen (Test 1). **(b) Nitrous oxide (Test 3 in Ref. [16]).**

Fig. 29 A representation of the chamber pressure and oxidizer mass flow rate during the burning time.

5 Conclusions

A phenomenological theory of the regression rate in axial injection end-burning hybrid rocket motors has been developed in the current work. The regression rate is composed of two components in this non-conventional configuration, one perpendicular to the gas flow and one parallel to it. The latter is the main topic of the paper, and the main dependencies on the motor operational parameters have been highlighted. The validation of the theoretical description is performed by a comparative study between firing tests using gaseous oxygen and nitrous oxide. A preliminary experimental analysis performed in a pressure-controlled combustion chamber displayed that the regression rate was strictly related to the chamber pressure, oxidizer mass flow rate, and port diameter. In particular, the sensitivity exponent on pressure increased from 1.48 for oxygen to 1.86 for nitrous oxide. This feature represented the benchmark of the physical model developed to highlight the physical quantities driving the regression rate. The accurate modelling of the regression rate relied on the correct evaluation of the flame stand-off distance from the top surface. The oxidizer mass flux, the chamber pressure, and the Reynolds number have been found to be crucial for the description of the flame distance. Four phenomena contributed to the effect of the pressure on this characteristic space: the mass diffusion, the kinetic reaction, thermal diffusivity, and turbulence. The theoretical analysis revealed that the sensitivity to pressure increased for nitrous oxide because of the decomposition mechanism occurring upstream of the flame front. Quantitative evaluations of the stand-off distance have been shown, which displayed that this was around 7 times longer with nitrous oxide than with oxygen, leading to a lower regression rate. A longer distance is required by nitrous oxide combustion than oxygen because the activation temperature of the N_2O thermal decomposition is higher than the activation temperature of the oxygen combustion with common hydrocarbons, leading to a strong reduction of the laminar flame speed. In addition, the diffusion of a larger amount of oxidizer is required with N_2O to achieve the stoichiometric condition with a further extension of the flame stand-off distance. Finally, a design methodology for the AIEB combustion chamber is illustrated, with a particular focus on the optimization of fuel mass loss and the design differences between the two oxidizers. An experimental campaign performed with the full configuration of AIEB employing a chocked nozzle displayed a reduced sensitivity of the regression rate on pressure due to the coupling of the oxidizer mass flow rate with the chamber pressure. This effect ensured the dynamic stability of the motor internal ballistics and a negligible reduction of the average mixture ratio in the case of nitrous oxide.

6 Acknowledgement

This research was supported by the Ministry of Education, Science, Sports and Culture Grants-in-Aid for Young Scientists and Japan Society for the Promotion of Science (JSPS).

Appendix A: Experimental Data

In this appendix, the reader can find the data list of the results displayed in Fig. 11 and Fig. 12. The measured regression rates at different operative conditions with both oxidizers are summed up in Table A.1. The measurement error of the pressure transducer is 0.044 MPa, while that of the mass flow meter is 0.009 L/min (which is equal to approximately 0.0002 g/s at ambient pressure for both oxidizers).

Regarding the regression rate, a rigorous error is difficult to determine because several error sources have been included in the measurement process. However, regression data are consistent with each other, and they have been validated by comparing them with the ratio of the grain length to the burning time (the end of the firing test coincides with the instant in which the flame reaches the fuel base).

Table A.1 Experimental axial regression rates obtained at different operating conditions with both the oxidizers.

Test	Oxidizer	Chamber pressure, MPa	Mass flow rate, g/s	Port diameter, mm	Regression rate, mm/s
1	O_2	0.10	0.259	3	0.75
2	O_2	0.10	0.346	3	0.67
3	O_2	0.10	0.117	3	1.09
4	O_2	0.10	0.143	3	1.04
5	O_2	0.10	0.196	3	0.79
6	O_2	0.11	0.078	2	0.74
7	O_2	0.40	0.030	0.5	2.84
8	O_2	0.40	0.121	1	2.58
9	O_2	0.41	0.485	2	3.15
10	O_2	0.41	1.093	3	4.55
11	O_2	0.90	0.068	0.5	5.23
12	O_2	0.90	0.272	1	5.44
13	O_2	0.91	1.088	2	5.48
14	O_2	1.00	0.217	1	8.33
15	O_2	1.01	0.325	1	4.87
16	O_2	1.01	0.545	1	4.21
17	O_2	1.01	0.431	1	4.82
18	O_2	1.01	0.650	1	3.73
19	O_2	1.01	0.762	1	3.60
20	O_2	1.01	0.874	1	3.27
21	O_2	1.40	0.106	0.5	8.05
22	O_2	1.41	1.692	2	8.21
23	O_2	1.88	0.574	1	10.04
24	O_2	2.39	0.181	0.5	13.31
25	O_2	2.41	0.725	1	13.38
26	O_2	2.89	0.219	0.5	15.42
27	O_2	2.89	0.876	1	15.21
28	O_2	3.37	1.027	1	17.25
29	O_2	3.39	0.257	0.5	17.94
30	N_2O	0.10	0.004	1.6	0.21
31	N_2O	0.10	0.014	1.6	0.08
32	N_2O	0.10	0.020	1.6	0.10
33	N_2O	0.11	0.167	4.6	0.14
34	N_2O	0.23	0.108	3.1	0.43
35	N_2O	0.32	0.593	3.0	0.29
36	N_2O	0.32	0.527	3.0	0.34
37	N_2O	0.42	0.078	1.8	0.50
38	N_2O	0.52	0.136	1.8	0.98
39	N_2O	0.62	0.317	3.0	0.91
40	N_2O	0.64	0.373	3.0	0.95
41	N_2O	0.69	0.291	1.8	0.79
42	N_2O	0.80	0.338	1.8	1.05
43	N_2O	0.85	1.250	3.0	1.10
44	N_2O	1.00	0.201	1.6	2.06
45	N_2O	1.08	0.086	0.8	1.38
46	N_2O	1.22	0.084	0.8	1.66
47	N_2O	1.24	0.115	0.8	1.55
48	N_2O	1.31	0.116	0.8	1.38
49	N_2O	1.36	0.116	0.8	1.50
50	N_2O	1.50	0.262	0.8	1.25
51	N_2O	1.50	0.069	0.8	2.42
52	N_2O	1.50	0.086	0.8	2.53
53	N_2O	1.51	0.197	0.8	1.60
54	N_2O	1.56	0.313	1.1	1.86
55	N_2O	1.61	0.291	1.2	2.24

56	N_2O	1.95	0.437	0.8	1.61
57	N_2O	2.00	0.263	0.8	2.17
58	N_2O	2.01	0.352	0.8	1.84

7 References

[1] T. Shimada, C. Carmicino, A. Karabeyoglu, Hybrid Rocket (Volume II), Aerospace 9 (2022) 233.

[2] C. Carmicino, Advances in Hybrid Rocket Technology and Related Analysis Methodologies, Aerospace 6 (2019) 128.

[3] A. Karabeyoglu, E. Toson, B. Evans, O/F Shift in Hybrid Rockets, AIAA Paper 2014-3851, July 2014.

[4] T. Kato, N. Hashimoto, H. Nagata, R. Akiba, I. Kudo, A Preliminary Study of End-Burning Hybrid Rocket, Part 1: Combustion Stability, J. Jpn. Soc. Aeronaut. Space Sci. 49 (2001) 33–39.

[5] F. Barato, M. Grosse, A. Bettella, Hybrid Rocket Fuel Residuals – An Overlooked Topic, AIAA Paper 2014-3753, July 2014.

[6] G. A. Marxman, M. Gilbert, Turbulent boundary layer combustion in the hybrid rocket, Symp. (Int.) Combust. 9 (1963) 371-383.

[7] G. A. Marxman, Combustion in the turbulent boundary layer on a vaporizing surface, Symp. (Int.) Combust. 10 (1965) 1337-1349.

[8] C. Carmicino, A. Russo Sorge, Experimental Investigation into the Effect of Solid-Fuel Additives on Hybrid Rocket Performance, J. Propuls. Power 31 (2015) 699-713.

[9] J. C. Thomas, F. A. Rodriguez, E. L. Petersen, Metallic Additives for Solid-Fuel Propulsion Applications, Combust. Sci. Technol. 195 (2023) 1279-1298.

[10] C. Nguyen, J. C. Thomas, Performance of Additively Manufactured Fuels for Hybrid Rockets, Aerospace 10 (2023) 500.

[11] J. C. Thomas, E. L. Petersen, HTPB Heat of Formation: Literature Survey, Group Additive Estimations, and Theoretical Effects, AIAA J. 60 (2022) 1269-1282.

[12] Y. Pal, S. K. Palateerdham, S. N. Mahottamananda, S. Sivakumar, A. Ingenito, Combustion Performance of Hybrid Rocket Fuels Loaded with MgB2 and Carbon Black Additives, Propul. Power Res. 12 (2023) 212-226.

[13] H. Nagata, H. Teraki, Y. Saito, R. Kanai, H. Yasukochi, M. Wakita, T. Totani, Verification Firings of End-Burning Type Hybrid Rockets, J. Propuls. Power 33 (2017) 1473–1477.

[14] Y. Saito, T. Yokoi, H. Yasukochi, K. Soeda, T. Totani, M. Wakita, H. Nagata, Fuel Regression Characteristics of a Novel Axial Injection End-Burning Hybrid Rocket, J. Propuls. Power 34 (2018) 247–259.

[15] Y. Saito, M. Kimino, A. Tsuji, Y. Okutani, K. Soeda, H. Nagata, High Pressure Fuel Regression Characteristics of Axial-Injection End Burning Hybrid Rockets, J. Propuls. Power 35 (2019) 1–14.

[16] R. Okuda, K. Komizu, A. Tsuji, T. Miwa, M. Fukada, S. Yokobori, K. Soeda, L. Kamps, H. Nagata, Fuel Regression Characteristics of Axial-Injection End-Burning Hybrid Rocket Using Nitrous Oxide, J. Propuls. Power 38 (2022) 759-770.

[17] T. Matsuoka, S. Murakami, H. Nagata, Transition characteristics of combustion modes for flame spread in solid fuel tube, Combust. Flame 159 (2012) 2466-2473.

[18] K. Komizu, Y. Saito, A. Tsuji, H. Nagata, Experimental Investigation of the Continuous Transition of Flame-Spreading near the Blow-Off Limit, J. Combust. 2020 (2020) 1-7.

[19] H. Nagata, H. Teraki, Y. Saito, R. Kanai, T. Totani, Verification Firings of End-Burning Type Hybrid Rockets, J. Propuls. Power 33 (2017) 1473-1477.
[20] N. Hashimoto, H. Nagata, T. Totani, I. Kudo, Determining factor for the blow-off limit of a flame spreading in an opposed turbulent flow in a narrow solid-fuel duct, Combust. Flame 147 (2006) 222-232.
[21] S. Heister, E. Wernimont, Hydrogen Peroxide, Hydroxyl Ammonium Nitrate, and Other Storable Oxidizers, Fundamentals of Hybrid Rocket Combustion and Propulsion, 1st ed., Progress in Astronautics and Aeronautics, edited by Chiaverini, M., and Kuo, K., Vol. 218, 2012, pp. 457– 487.
[22] Saito Y., Yokoi T., Neumann L., Yasukochi H., Soeda K., Totani T., Wakita M., Nagata H., Investigation of Axial-Injection End-Burning Hybrid Rocket Motor Regression, Adv. Aircr. Spacecr. Sci. 4 (2017) 281-296.
[23] L. Carmignani, Flame Tracker: An Image Analysis Program to Measure Flame Characteristics, SoftwareX 15 (2021) 100791.
[24] M. Chiaverini, Review of Solid-Fuel Regression Rate Behavior in Classical and Nonclassical Hybrid Rocket Motors, Fundamentals of Hybrid Rocket Combustion and Propulsion, Progress in Astronautics and Aeronautics, edited by Chiaverini, M., and Kuo, K., 2007, pp. 37– 126.
[25] G. Gallo, L. Kamps H. Shota, C. Carmicino, H. Nagata, Numerical Model for the Fuel Regression-Rate Prediction in Hybrid Rockets Fed by Liquid Nitrous Oxide, Combust. Flame 259 (2024) 113160.
[26] G. Gallo, L. Kamps, H. Shota, C. Carmicino, H. Nagata, Numerical Model for the Prediction of the Regression Rate in Hybrid Rocket Kick-Motors Working with Nitrous Oxide, AIAA Paper 2023-2348, January 2023.
[27] M. W. Beckstead, R. L. Derr, C. F. Price, A model of composite solid-propellant combustion based on multiple flames, AIAA J. 8 (1970) 2200–2207.
[28] B. Rasmussen, R. A. Frederick, Nonlinear Heterogeneous Model of Composite Solid-Propellant Combustion, J. Propuls. Power 18 (2002) 1086–1092.
[29] D. Bianchi, F. Nasuti, C. Carmicino, Hybrid Rockets with Axial Injector: Port Diameter Effect on Fuel Regression Rate, J. Propuls. Power 32 (2016) 984-996.
[30] Y. Pizzo, C. Lallemand, A. Kacem, A. Kaiss, J. Gerardin, Z. Acem, P. Boulet, B. Porterie, Steady and transient pyrolysis of thick clear PMMA slabs, Combusti. Flame 162 (2015) 226-236.
[31] S. H. Chung, Stabilization, propagation and instability of tribrachial triple flames, Proc. Combust. Inst. 31 (2007) 877-892.
[32] T. Gautam, Lift-off Heights and Visible Lengths of Vertical Turbulent Jet Diffusion Flames in Still Air, Combust. Sci. Technol. 41 (1984) 17-29.
[33] Q. Wang, L. Hu, S. H. Chung, Blow-out of non-premixed turbulent jet flames at sub-atmospheric pressures, Combust. Flame 176 (2017) 358–360.
[34] H. Kobayashi, Experimental study of high-pressure turbulent premixed flames, Exp. Therm. Fluid Sci. 26 (2002) 375–387.
[35] S. P. R. Muppala, N. K. Aluri, F. Dinkelacker, A. Leipertz, Development of an algebraic reaction rate closure for the numerical calculation of turbulent premixed methane, ethylene, and propane/air flames for pressures up to 1.0 MPa, Combust. Flame 140 (2005) 257–266.

[36] S. Gordon, B. J. McBride, Computer program of complex chemical equilibrium compositions and applications, NASA Reference Publication 1311, 1994.
[37] A. Karabeyoglu, J. Dyer, J. Stevens, B. Cantwell, Modeling of N2O Decomposition Events, AIAA Paper 2008-4933, July 2008.
[38] R. M. Lewis, C. N. Hinshelwood, The Thermal Decomposition of Nitrous Oxide, Proceeding of the Royal Society of London. Series A, Vol. 168, pp. 441-454, 1938.
[39] A. Coronetti, W. A. Sirignano, Numerical Analysis of Hybrid Rocket Combustion, J. Propuls. Power 29 (2013) 371-384.
[40] G. P. Sutton, O. Biblarz, Solid Rocket Components and Motor Design, Rocket Propulsion Elements, 7th ed., John Wiley & Sons, 2001.